Available online at www.sciencedirect.com

ScienceDirect

Geochimica et Cosmochimica Acta 301 (2021) 91–115

Geochimica et Cosmochimica Acta

www.elsevier.com/locate/gca

Isotopic fractionation accompanying CO_2 hydroxylation and carbonate precipitation from high pH waters at The Cedars, California, USA

John N. Christensen [a,*], James M. Watkins [b], Laurent S. Devriendt [b,c], Donald J. DePaolo [a,d], Mark E. Conrad [a], Marco Voltolini [a], Wenbo Yang [e], Wenming Dong [a]

[a] *Earth and Environmental Science Area, Energy Geosciences Division, Lawrence Berkeley National Laboratory, Berkeley, CA 94720, United States*

[b] *Department of Earth Sciences, University of Oregon, Eugene, OR 97403, United States*

[c] *Department of Ocean System Sciences, Royal Netherlands Institute for Sea Research (NIOZ), and Utrecht University, Texel, the Netherlands*

[d] *Department of Earth and Planetary Science, University of California, Berkeley, CA 94720, United States*

[e] *Department of Integrative Biology, University of California, Berkeley, CA 94720, United States*

Received 11 November 2019; accepted in revised form 2 January 2021; Available online 12 January 2021

Abstract

The Cedars ultramafic block hosts alkaline springs (pH > 11) in which calcium carbonate forms upon uptake of atmospheric CO_2 and at times via mixing with surface water. These processes lead to distinct carbonate morphologies with "floes" forming at the atmosphere-water interface, "snow" of fine particles accumulating at the bottom of pools and terraced constructions of travertine. Floe material is mainly composed of aragonite needles despite $CaCO_3$ precipitation occurring in waters with low Mg/Ca (<0.01). Precipitation of aragonite is likely promoted by the high pH (11.5–12.0) of pool waters, in agreement with published experiments illustrating the effect of pH on calcium carbonate polymorph selection.

The calcium carbonates exhibit an extreme range and approximately 1:1 covariation in $\delta^{13}C$ (−9 to −28‰ VPDB) and $\delta^{18}O$ (0 to −20‰ VPDB) that is characteristic of travertine formed in high pH waters. The large isotopic fractionations have previously been attributed to kinetic isotope effects accompanying CO_2 hydroxylation but the controls on the $\delta^{13}C$-$\delta^{18}O$ end-members and slope have not been fully resolved, limiting the use of travertine as a paleoenvironmental archive. The limited areal extent of the springs (~0.5 km^2) and the limited range of water sources and temperatures, combined with our sampling strategy, allow us to place tight constraints on the processes involved in generating the systematic C and O isotope variations.

We develop an isotopic reaction–diffusion model and an isotopic box model for a CO_2-fed solution that tracks the isotopic composition of each dissolved inorganic carbon (DIC) species and $CaCO_3$. The box model includes four sources or sinks of DIC (atmospheric CO_2, high pH spring water, fresh creek water, and $CaCO_3$ precipitation). Model parameters are informed by new floe $\Delta^{44}Ca$ data (−0.75 ± 0.07‰), direct mineral growth rate measurements (4.8 to 8 × 10^{-7} mol/m^2/s) and by previously published elemental and isotopic data of local water and DIC sources. Model results suggest two processes control the extremes of the array: (1) the isotopically light end member is controlled by the isotopic composition of atmospheric CO_2 and the kinetic isotope fractionation factor (KFF (‰) = (α − 1) × 1000) accompanying CO_2 hydroxylation, estimated here to be −17.1 ± 0.8‰ (vs. $CO_{2(aq)}$) for carbon and −7.1 ± 1.1‰ (vs. '$CO_{2(aq)} + H_2O$') for oxygen at 17.4 ± 1.0 °C. Combining our results with revised CO_2 hydroxylation KFF values based on previous work suggests consistent KFF values of −17.0 ± 0.3‰ (vs. $CO_{2(aq)}$) for carbon and −6.8 ± 0.8‰ for oxygen (vs. '$CO_{2(aq)} + H_2O$') over the 17–28 °C temperature

* Corresponding author.
E-mail address: jnchristensen@lbl.gov (J.N. Christensen).

https://doi.org/10.1016/j.gca.2021.01.003

range. (2) The isotopically heavy endmember of calcium carbonates at The Cedars reflects the composition of isotopically equilibrated DIC from creek or surface water (mostly HCO_3^-, pH = 7.8–8.7) that occasionally mixes with the high-pH spring water. The bulk carbonate $\delta^{13}C$ and $\delta^{18}O$ values of modern and ancient travertines therefore reflect the proportion of calcium carbonate formed by processes (1) and (2), with process (2) dominating the carbonate precipitation budget at The Cedars. These results show that recent advances in understanding kinetic isotope effects allow us to model complicated but common natural processes, and suggest ancient travertine may be used to retrieve past meteoric water $\delta^{18}O$ and atmospheric $\delta^{13}C$ values. There is evidence that older travertine at The Cedars recorded atmospheric $\delta^{13}C$ that predates large-scale combustion of fossil fuels.

Keywords: Calcium isotopes; Carbon isotopes; Oxygen isotopes; Calcite; Aragonite; Alkaline springs; CO_2 hydroxylation; Kinetic isotope effects

1. INTRODUCTION

Most Earth-surface carbonate minerals precipitate out of stable isotope equilibrium with their host aqueous solution (Coplen, 2007; Watkins et al., 2013, 2014; Devriendt et al., 2017; Daëron et al., 2019). Deviations from isotopic equilibrium are manifested in a variety of ways. One of the most striking ways, still not fully understood, is a strong correlation between $\delta^{13}C$ and $\delta^{18}O$ in carbonates precipitated under different circumstances, from marine calcifying organisms (e.g., McConnaughey, 1989; Spero et al., 1997; Adkins et al., 2003; Kimball et al., 2014; Hermoso et al., 2014; Chen et al., 2018) to cryogenic calcium carbonates (Clark and Lauriol, 1992; Žák et al., 2008), lacustrine carbonates (Talbot, 1990), and speleothem carbonates formed by CO_2 degassing (Daëron et al., 2011; Tremaine et al., 2011). The slope of the $\delta^{13}C$-$\delta^{18}O$ covariation varies because kinetic isotope effects in the $CaCO_3$-DIC-H_2O system are sensitive to factors such as temperature, solution pH, mixing between DIC reservoirs, the residence time of DIC in solution, whether CO_2 is ingassing or outgassing from solution, and whether the system is open versus closed (e.g. McConnaughey, 1989; Clark et al., 1992; Falk et al., 2016; Devriendt et al., 2017; Chen et al., 2018).

Calcium carbonates formed in hyperalkaline springs exhibit some of the largest and most systematic variations in $\delta^{13}C$ and $\delta^{18}O$ (O'Neil and Barnes, 1971; Clark and Fontes, 1990; Clark et al., 1992; Meister et al., 2011; Leleu et al., 2016; Falk et al., 2016). The archetype locality is a set of carbonate formations precipitating from springs emanating from serpentinized peridotite in the Samail ophiolite, Sultanate of Oman (Barnes et al., 1978; Clark et al., 1992; Kelemen et al., 2011; Mervine et al., 2014; Falk et al., 2016). Fig. 1 (data from Clark and Fontes, 1990; Clark et al., 1992; Falk et al., 2016; Mervine et al., 2014) shows the strong $\delta^{13}C$-$\delta^{18}O$ correlation spanning a range of about 25‰ in both ^{13}C and ^{18}O, with most of the values being isotopically lighter than the expected equilibrium values. The isotopically light endmember of the $\delta^{13}C$-$\delta^{18}O$ array has been attributed to hydroxylation of dissolved CO_2 ingassing from the atmosphere (Clark et al., 1992). The rest of the array has been attributed to some combination of mixing between different DIC sources, partial equilibration of DIC, and post-depositional recrystallization (Falk et al., 2016). Recent developments of numerical models that quantify kinetic isotope effects in the $CaCO_3$-DIC-H_2O system (Devriendt et al., 2017; Sade and Halevy, 2017; Chen et al., 2018) provide an opportunity to gain a quantitative understanding of the peculiar and large kinetic isotope effects in high pH environments.

The calcium carbonate samples from Oman represented in Fig. 1 were collected over an area of 50 × 200 km from calcium-hydroxide springs (pH = 11.2–12.1) spanning a large range in temperature (22–32 °C), in $\delta^{13}C$ of DIC surface and ground waters, and in the age of samples (0–40 ka). This explains the large range of possible equilibrium calcite values (Fig. 1). In this study, we investigate a similar high-pH system, The Cedars, where the springs are within a 0.5 km^2 area, the spring waters have a more constant temperature (17.4 ± 1.0 °C) and $\delta^{13}C$ value. Our approach is to determine the calcite and aragonite growth rates using Ca isotopes and detailed field observations to evaluate calcium carbonate $\delta^{13}C$ and $\delta^{18}O$ values in the context of these mineral growth rate data, solution chemistry, travertine forms, and carbon sources/transport.

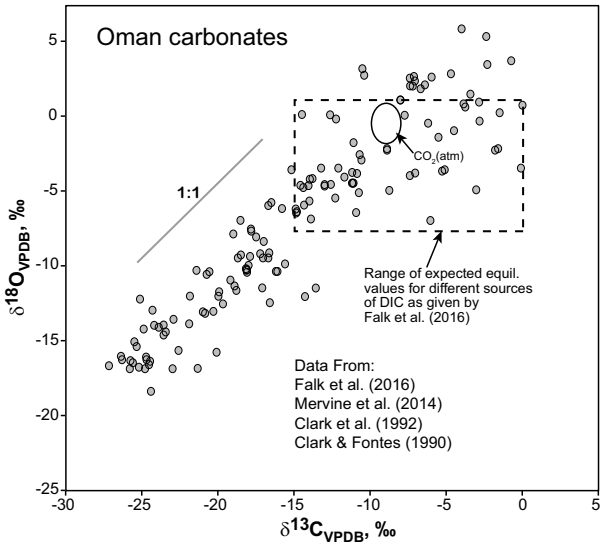

Fig. 1. $\delta^{13}C$ vs. $\delta^{18}O$ of carbonates associated with high pH springs in Oman emanating from ultramafic rocks of the Samail ophiolite.

2. THE CEDARS

The Cedars (aka Cazadero; Barnes et al. 1967) peridotite is a relatively small tectonically emplaced fault-bounded wedge of ultramafic rock located in the California Coast Range north of San Francisco (Coleman 2000; Blake et al., 2012; Fig. 2). The dominant rock type is harzburgite with lesser amounts of dunite. This fragment of Jurassic age oceanic lithosphere has been inferred to be an obducted abyssal peridotite from an oceanic fracture zone (Coleman 2000), or alternatively as the basal peridotite of the Coast Range Ophiolite formed in the mantle wedge above the Mesozoic California-margin subduction zone (Choi et al. 2008). The central portion of The Cedars is partially serpentinized while the margins consist of sheared serpentinite (Blake et al. 2012). The Cedars ultramafic body is in fault contact with Franciscan Complex mélange greywacke and shale (Coleman 2000). It has a dipping, wedge-shaped structural geometry, extending to a depth of 4 km but with an average thickness of 2 km or less (Blake et al. 2002).

A series of springs emerge along the course of Austin Creek at the bottom of the main canyon between ~275 m and 335 m elevation. Some springs produce pools and terraced deposits adjacent to the creek before emptying into the creek. At other locations springs enter the creek directly from the bottom. An example at the Barnes Spring Complex (BSC, Fig. 2) of a spring-fed pool adjacent to Austin Creek is shown in Fig. 3. The unusual nature of the springs at The Cedars was first recognized and described by Barnes et al. (1967) and Barnes and O'Neil (1969). They found that the springs produce ultrabasic waters (pH = 11.7) with low DIC, Mg, Fe, and silica concentrations but a relatively high Ca concentration. They attribute the spring water's unusual chemical characteristics to on-going serpentinization of primary ultramafic rock at shallow depth. Isotope studies demonstrated that the spring waters have a meteoric origin as opposed to an ancient connate origin from the underlying Franciscan formation (Barnes and O'Neil, 1969; Barnes et al. 1978), and that calcium carbonates precipitating from the ultrabasic waters have unusually low $\delta^{13}C$ and $\delta^{18}O$ values (O'Neil and Barnes, 1971).

Morrill et al. (2013) conducted a more extensive study of the high pH waters of The Cedars. They identified two types of ultrabasic water that variably mix: (1) waters with deep flow paths that interacted with the underlying Franciscan Complex enriching the waters in K^+, other salts and volatile organic compounds before encountering ultramafic rock, and (2) waters with shallow paths that pass solely through ultramafic rock and are characterized by lower salinity and $[K^+]$. The springs exhibit stable temperatures with time and season (spring *vs.* fall), averaging 17 ± 1 °C (Morrill et al., 2013; Suzuki et al., 2013). Tritium dating of water samples by Suzuki et al. (2017) indicates that water with deep flow paths, as at the Grotto Pool Springs, has an age greater than 60 years (<0.8 Tritium units, TU), while

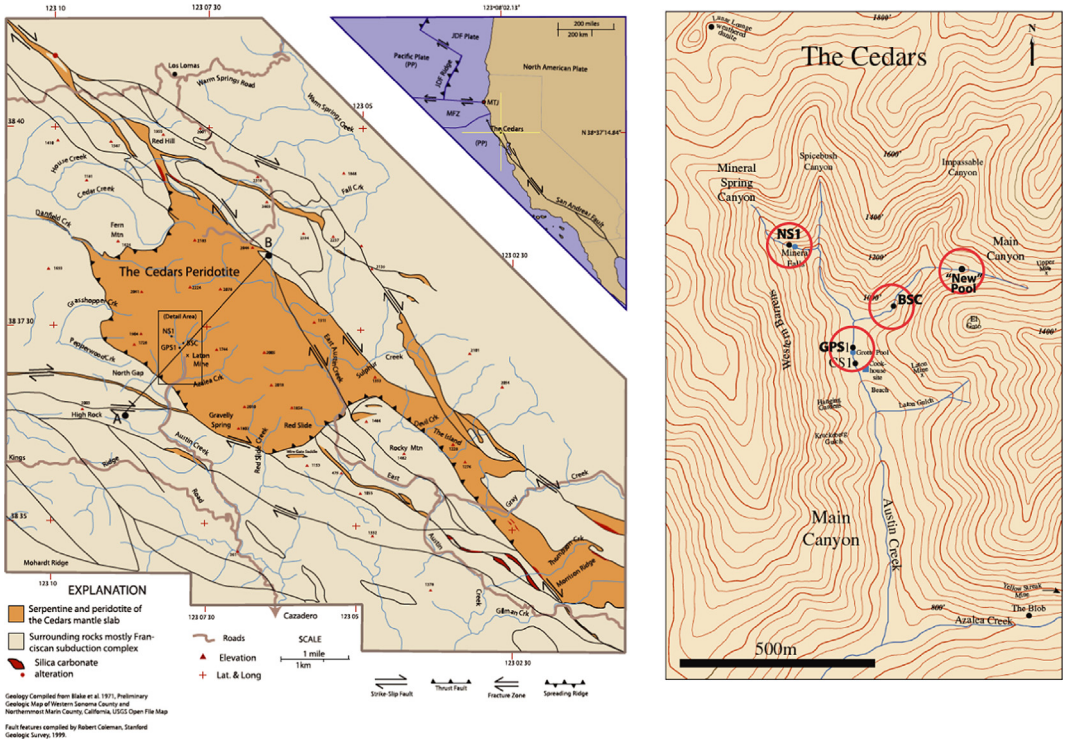

Fig. 2. Maps showing the location of The Cedars and sampling locations (modified after Morrill et al. 2013). Using the nomenclature of Morrill et al. (2013), BSC = Barnes Spring Complex, GPS = Grotto Pool Springs. The Wedding Cake is at the NS1 locality above Mineral Falls.

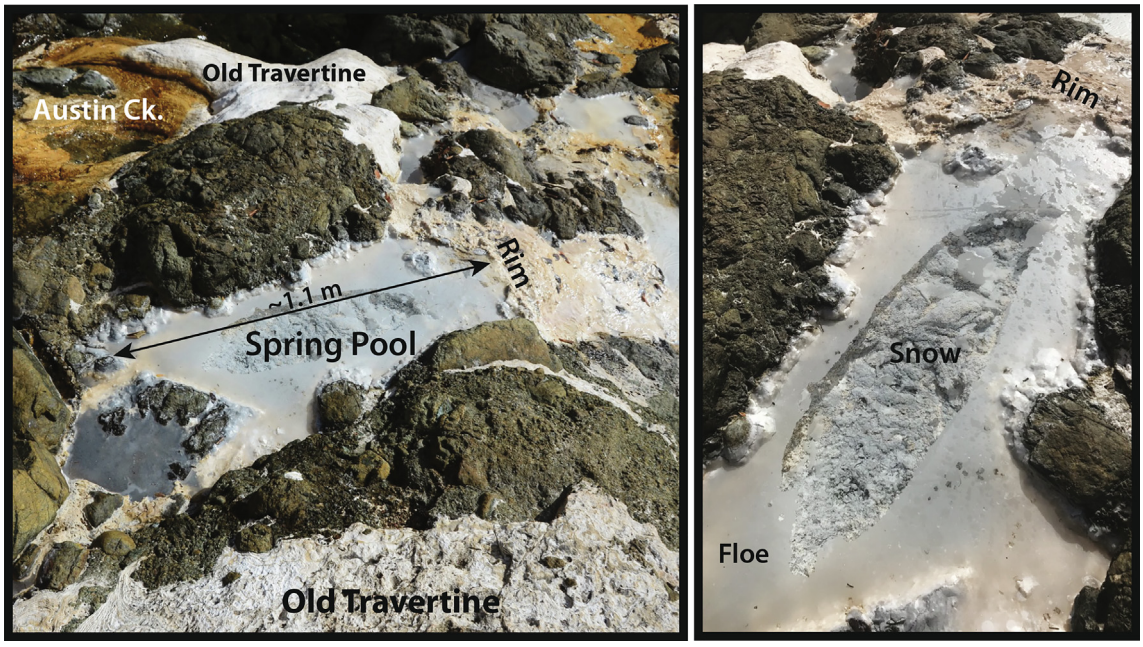

Fig. 3. Photos of a spring pool adjacent to Austin Creek at the Barnes Spring Complex (BSC) taken in October, 2018. The left panel shows examples of Ca-carbonate floe at the pool surface (much floe has been cleared away in sample collection, giving a view of the pool bottom), Ca-carbonate snow at the bottom of the pool, the Ca-carbonate rim of the pool where water exits the pool, and old travertine deposits. The dark outcrops are ultramafic rocks of The Cedars. The right panel shows a closer view from a different angle of the pool featured in the left panel.

Barnes Complex spring water, with an inferred shallow flow path, gave a value of 2.3 TU, possibly indicating an age younger than 10 years since that value is similar to contemporaneous Bay Area precipitation (1.3–2.2 TU, Harms 2015).

3. METHODS

3.1. Sampling

Samples were collected on eight visits to The Cedars in 2013, 2014, 2016 and 2018. Four sites were sampled (Fig. 2): (1) The Wedding Cake above Mineral Falls, (2) The Barnes Spring Complex (BSC), (3) Grotto Pool Springs (GPS), and (4) "New" Pool within Austin Creek ~ 250 m upstream of BSC. Water samples from the high pH springs and from Austin Creek were filtered to 0.22 μm using Durapore filter units (Millipore), collected in HDPE bottles and acidified to pH 2 using high purity HNO_3 (Baseline Nitiric Acid, Seastar Chemicals). Prior to collection, the pH of the sampling source was measured with an Orion hand-held pH meter (Thermo Scientific). Samples of calcium carbonate collected are of several types as illustrated in Fig. 3: (1) partially consolidated material from rims of pools; (2) precipitates from the surfaces of pools (called here floes); (3) dendritic forms and encrustations from sites of creek-spring mixing; (4) unconsolidated material (called here snow) from pool bottoms; and (5) solid, old travertine deposits. Surface floes were either skimmed from the surface or captured on screens.

3.2. Analytical Methods

Below are brief descriptions of the analytical techniques used in this study. Further details are provided in Supplementary material.

Samples of calcium carbonate and water were analyzed for calcium isotope composition using thermal ionization mass spectrometry on a Triton (ThermoFisher) multicollector instrument. Prior to chemical separation, samples were spiked with a ^{42}Ca-^{48}Ca double spike. The Ca isotope results ($\delta^{44}Ca$) are reported as per mil deviations of the $^{44}Ca/^{40}Ca$ ratio from Bulk Silicate Earth (BSE; Nielsen et al. 2011). Our measurements confirm the BSE reference $^{44}Ca/^{40}Ca$ ratio is $0.96 \pm 0.05‰$ higher than the value for SRM915a.

Oxygen and carbon isotope analyses of carbonate samples were conducted in the Center for Stable Isotope Biogeochemistry (CSIB), Department of Integrative Biology, University of California, Berkeley, using a GV IsoPrime mass spectrometer equipped with Dual-Inlet and MultiCarb systems. Results are reported relative to Vienna Pee Dee Belemnite (VPDB). The overall external analytical precision is ±0.05‰ for $\delta^{13}C$ and ±0.07‰ for $\delta^{18}O$.

Elemental concentrations of the water samples were determined by Quadrupole-ICPMS (Elan DRC II, PerkinElmer SCIEX, USA). Images of calcium carbonate samples were obtained with a Zeiss EVO-LS10® scanning electron microscope (SEM), with capabilities of secondary electron (SE) imaging and back-scattered electron (BSE) imaging. Phase identification and quantification in selected solid samples were carried out via X-Ray powder diffrac-

tion (XRPD) with a Rigaku SmartLab® X-ray diffractometer.

4. RESULTS

4.1. XRPD and SEM observations

Fourteen carbonate samples were selected for XRPD analysis to cover the observed range in sample textures. The fractions of the identified mineral phases are given in Table 1. Aragonite and/or calcite are found in all samples, with aragonite ranging from 18% to 99.7%, and calcite ranging from 0.14% to 82%. Small amounts of vaterite (a polymorph of Ca carbonate) were identified in one floe sample (BSC Carb I: 0.5 ± 0.2%) and in one sample of a pool edge (BSC PE-C2 crust: 0.6 ± 0.2%). Brucite ($Mg(OH)_2$) was found in some samples of BSC pool edges (PB-C2 and PE-C2: 3 and 8%, respectively), in a filtered snow sample from BSC (PB-1: 6.8%), a GPS pool (Carb K: 0.5%) and in one of the samples from mixed spring-creek water (Carb AA: 7.7%). In samples of snow filtered from GPS pool water, both hydromagnesite (Carb J; 27%; Carb K: 49.5%) and nitromagnesite (Carb J; 4.5%; Carb K: 2.3%) were detected. Nesquehonite ($MgCO_3{\cdot}3H_2O$) was also detected in one sample (Carb K: 3%).

SEM images of a sample taken from the rim of a pool (Carb A, Fig. S1) show elongate crystals up to 10–15 μm of aragonite (as identified by the XRPD analysis) gathered in bundles, sprays and spheres. The samples from the New Pool (Carb B and Carb C) affected by creek mixing, is also identified by XRPD as 100% aragonite, and consist of sharp needles up to at least 40 μm grouped in radial sprays or spheres (Fig. S2 and S3). Both the soft encrustation on rock and the elongate branching forms display similar micro-textures.

The samples of floes have a more varied mineralogy and texture than samples from the Wedding Cake and from the New Pool. Fig. 4 compares the inferred top (upwards from water) and bottom (down into the water) surfaces of floe carbonates from a BSC pool. The top-side of the floe (Fig. 4A) displays radiating horizontal sprays of aragonite crystals, forming a relatively flat surface. In contrast, the bottom side (Fig. 4B) is rougher, with the terminations of the aragonite sprays forming a hummocky surface. Calcite rhombohedra are scattered across this surface, apparently forming largely after growth of the aragonite sprays. Open areas constitute approximately 15–20% of the area of this floe sample (Carb. D). Fig. S4 provides views of the broken edges of this floe material (Carb D). In the cross-sections the aragonite sprays can be seen to radiate from points, forming intersecting hemispheres. In this case the floe has a thickness of about 10 to 12 μm. Similar differences between the tops and bottoms of floes are confirmed by examination of carefully collected samples so that flakes of known original orientation could be examined by SEM (Fig. 4C).

The growth rate of the floes was determined by measuring the thickness as a function of time. After eight days of carbonate growth, floe thickness was 20–25 μm, as determined using SEM images of oriented fragments (Fig. 5).

Table 1
XRPD results for mineral compositions of carbonate samples.

Label	Description	Aragonite, %	Calcite, %	Vaterite, %	Hydromagnesite, %	Nitromagnesite, %	Brucite, %	Nesquehonite, %
Carb A	Wedding Cake rim	99.7 ± 0.4	0.27 ± 0.06	n.d.	n.d.	n.d.	n.d.	n.d.
Carb B	New Pool Xtl String	99.7 ± 0.4	0.29 ± 0.05	n.d.	n.d.	n.d.	n.d.	n.d.
Carb H	Floe GPS1	17.8 ± 0.3	82.2 ± 0.50	n.d.	n.d.	n.d.	n.d.	n.d.
Carb I	Floe BSC	21.7 ± 0.6	77.8 ± 0.90	0.5 ± 0.2	n.d.	n.d.	n.d.	n.d.
Carb J	GPS filtered snow (pool 1)	68.0 ± 0.5	0.14 ± 0.06	n.d.	27.4 ± 0.8	4.5 ± 0.4	n.d.	n.d.
Carb K	GPS filtered snow (pool 2)	25.0 ± 0.2	19.8 ± 0.20	n.d.	49.5 ± 0.5	2.3 ± 0.2	0.5 ± 0.1	3.0 ± 0.1
Carb AA	Mixed spr/ck water at BSC	91.0 ± 0.4	1.30 ± 0.08	n.d.	n.d.	n.d.	7.7 ± 0.4	n.d.
BSC	Floe from pool A, BSC. Powder	91.5 ± 0.2	8.51 ± 0.09	n.d.	n.d.	n.d.	n.d.	n.d.
BSC	Floe from pool A, BSC. Sheet	55.2 ± 0.5	45.0 ± 3.00	n.d.	n.d.	n.d.	n.d.	n.d.
PB-C1	Pool B snow, from bottom	86.0 ± 0.8	7.10 ± 0.20	n.d.	n.d.	n.d.	6.8 ± 0.2	n.d.
PB-C2 bulk	Edge pool B, BSC. Whole sample	91.1 ± 0.7	0.53 ± 0.04	n.d.	n.d.	n.d.	8.4 ± 0.6	n.d.
PB-C2 crust	Edge pool B, BSC. Outer surface	46.2 ± 0.2	48.8 ± 0.80	n.d.	n.d.	n.d.	5.0 ± 0.2	n.d.
PE-C2 bulk	Edge pool E, BSC. Whole sample	91.0 ± 0.6	5.90 ± 0.10	n.d.	n.d.	n.d.	3.1 ± 0.1	n.d.
PE-C2 crust	Edge pool E, BSC. Outer surface	77.5 ± 0.4	17.9 ± 0.09	0.6 ± 0.2	n.d.	n.d.	4.1 ± 0.2	n.d.

In the inset to Fig. 5, a piece of floe collected after four days of growth shown at the same scale has half the thickness of the eight-day growth, suggesting a constant linear growth rate of about 3 μm/day.

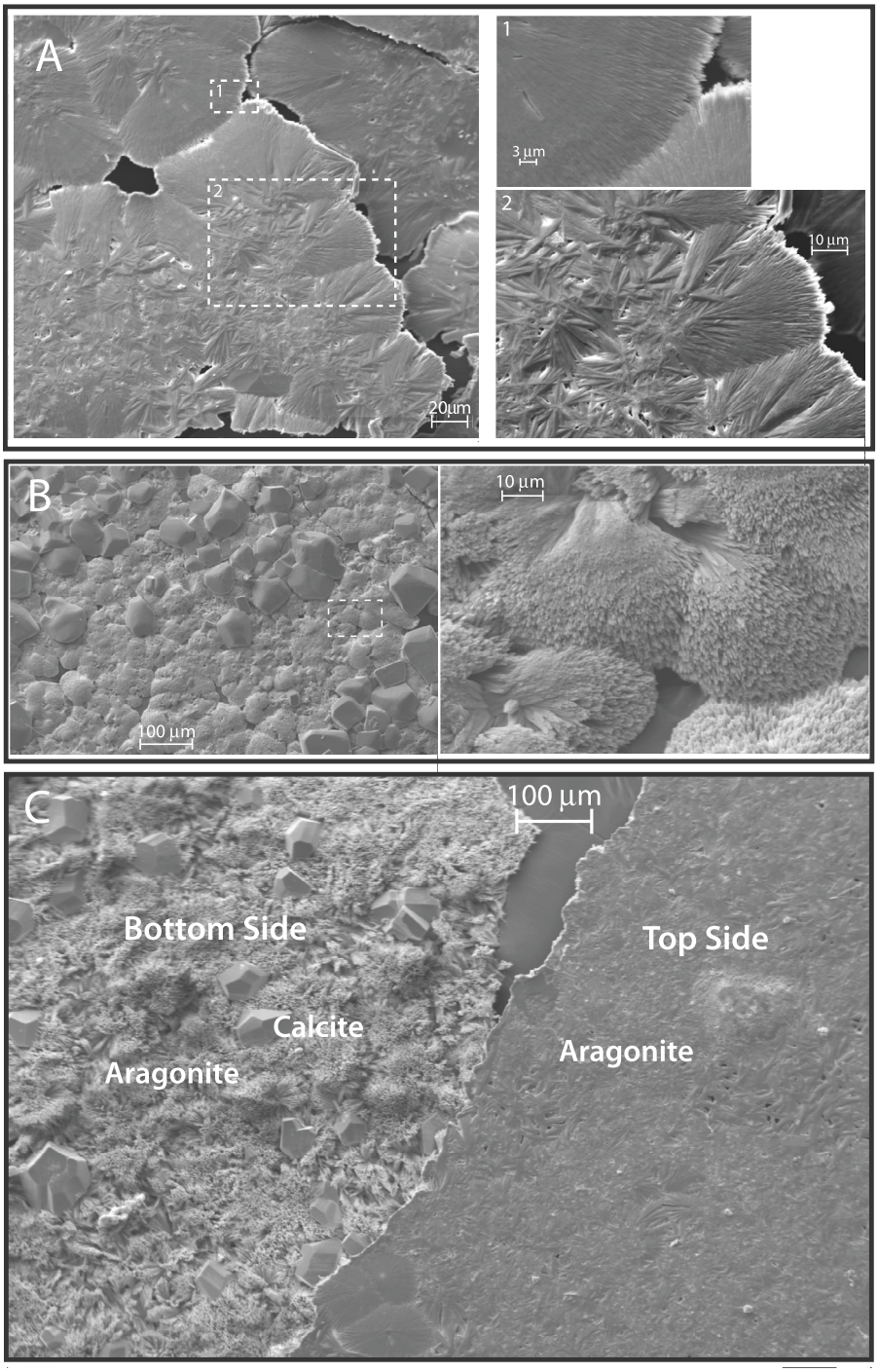

Fig. 4. SEM images of floe calcium carbonate from BSC pool surface. **(A)** Image of the inferred top side of the floe (Carb D). Texture consists of radiating crystals of aragonite (identified in XRPD) in a horizontal plane (detail in inset 1), showing in places a plumose/branching texture (inset 2). **(B)** The inferred bottomside of the floe. To right is an enlargement of the area in the dashed box in the left panel. Left image show calcite rhombs on sprays of aragonite crystals. In contrast to the side shown in A, this side is hummocky and less smooth. In this example, there are open areas between aragonite sprays representing approximately 10–15% of the area of the floe. **(C)** SEM image comparing the top and bottom sides of an another example of floe carbonate (flakes were placed next to each other in opposite orientations) from the Barnes Complex. In this case the material was collected to preserve the original orientation of the sample.

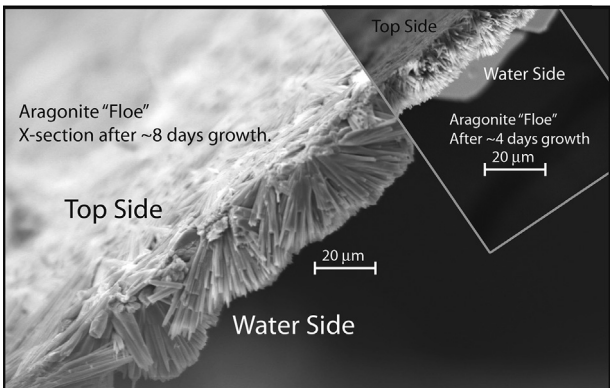

Fig. 5. SEM images showing cross sections of BSC floe material representing approximately eight days of growth and (inset) four days of growth. The top side is to the left, and the bottom side (facing down into the pool water) to the right. The 8-day image shows a thickness of 20–25 microns, with about half that thickness after four days growth, suggesting a constant growth rate of ~3 microns/day.

Sparse florets of hydromagnesite (identified by EDS and morphology) can be found at or partially embedded into the surfaces of calcite rhombs (Fig. S5), indicating that hydromagnesite is a trace and late-precipitating phase but can be contemporaneous with calcite growth. Other observed features include co-occurring smooth calcite rhomb faces together with rough micro-stepped saddles (Fig. S6) suggestive of the effects of bacterially exuded bio-polymers (e.g. Lian et al. 2006; Tourney and Ngwenya 2009), associations with apparent bacterial colonies (Fig. S7) and aragonite needles featuring stacked steps of hexagonal plates (Fig. S8) that are suggestive of surface nucleation control of growth.

From the above observations, we infer the following growth stages for floes forming at the surface of high pH pools:

1. Nucleation of aragonite crystals, with horizontal sprays of aragonite crystals suspended by surface tension and forming the base for layer formation.
2. Bundles of aragonite crystals grow parallel to the water surface and downward into the water, forming hemispheres of crystals that merge to form a nearly continuous layer.
3. After aragonite, blocky rhombohedral calcite crystals form, nestled among aragonite hemispheres. Calcite can be seen overgrowing aragonite needles.
4. Late, but accompanying calcite growth, precipitation of hydromagnesite, $Mg_5(CO_3)_4(OH_2)\cdot(H_2O)_4$ or Dypingite, $Mg_5(CO_3)_4(OH_2)\cdot(H_2O)_5$.
5. Eventually the floe sinks to the bottom of the pool when a mechanical disturbance breaks the surface tension (see suppl. mat. for the limit of surface tension on floe thickness). After sinking to the bottom of the pool, calcite growth can continue on the surface of broken floe fragments.

4.2. Chemistry of water samples

Elemental concentrations of water samples along with pH are presented in Table 2. The direct samples of springs and of pools have pH in the range of 11.3–12, and are characterized by relatively high Ca concentrations (12–58 ppm), high K concentrations (0.5–7 ppm), and low Mg concentrations (0.07–0.35 ppm). In contrast, samples of Austin Creek have pH in the range of 7.8–9.5 and are characterized by relatively low Ca concentrations (1.2–8 ppm), low K concentrations (0.06–0.7 ppm) and high Mg concentrations (41–49 ppm). The pool and spring water samples with pH $\geq$ 11.3 mostly have very low Mg/Ca molar ratios, less than 0.01, except for two samples of the Wedding Cake pool that have Mg/Ca ratios of 0.34 and 4.5. The creek samples have high Mg/Ca ranging from 8.5 to 66, which varies with pH, suggestive of mixing between creek water and spring water. Mixing models between creek water and spring water fit well the water samples with pH < 11 (Fig. 6), indicating that the chemical influence of spring water can be discerned in downstream creek samples.

4.3. δ^{44}Ca of water samples

The high pH water samples range in δ^{44}Ca from 0.02‰ up to 1.23‰. The low end of the range is similar to the δ^{44}Ca of upper mantle peridotite (Huang et al., 2010) consistent with the Ca in the springs being derived from the serpentinization of the ultramafic rocks. The sample with the highest Ca concentration (58 ppm, Wedding Cake Seep) also has the lowest δ^{44}Ca (0.02 ± 0.06‰), while the sample with the lowest Ca concentration (12 ppm, Wedding Cake Pool) has the highest δ^{44}Ca (1.23 ± 0.06‰). This pattern in concentration and δ^{44}Ca suggests an effect due to precipitation of calcium carbonate at the various sampling localities and times. To examine this, the isotopic data for the waters with pH > 11 (F1-F4, F7-F15) are used for Rayleigh distillation calculations (Fig. 7A). The slope of the best-fit line to the data ($r^2 = 0.91$, $p < 0.01$) gives a calcium fractionation factor ($\sim\Delta^{44}Ca = \delta_{CaCO_3}$-$\delta_{water}$) of -0.76 ± 0.12‰ (2σ), indicating that this is the average Ca isotope fractionation accompanying the removal of Ca^{2+} to calcium carbonate from the various waters at The Cedars. Below we compare this value to results for Δ^{44}Ca derived from direct water/$CaCO_3$ differences.

4.4. δ^{44}Ca of calcium carbonate samples

The Ca isotope ratios (δ^{44}Ca) of the calcium carbonates range from −0.77‰ to −0.17‰ (Table 3), with no correlation with either δ^{13}C or δ^{18}O (Fig. S9). The analyzed carbonates cover a range of textures and mineralogy. Because of their immediate association with water, the floe samples provide the best opportunities to directly measure fractionation (Δ^{44}Ca) between calcium carbonate and dissolved Ca^{2+} arising from crystallization. We analyzed five water-floe pairs (Table 4), three from different pools at the BSC, and one each from the Wedding Cake and from the GPS. The average of all five pairs gives a Δ^{44}Ca of

Table 2
Ca isotopic and chemical compositions of waters from The Cedars.

Label	Location	$\delta^{44}Ca_{BSE}$, ‰	±2σ	Ca, ppm*	K, ppm	Mg, ppm	Na, ppm	Sr, ppb	Mg/Ca molar	pH_{NBS}
F1	GPS pool under floe	0.26	0.16	34.9	6.98	0.07	342	1.41	0.0031	12.0
F2	BC spring	0.18	0.12	51.7	1.22	0.07	49	5.23	0.0020	11.8
F3	Wedding Cake Pool	1.23	0.06	12.2	0.54	34.8	14	0.79	4.53	11.3
F4	BC1 pool under floe	0.16	0.06	51.1	1.36	0.11	50	3.16	0.0033	11.5
F5	Ck inflow to New Pool	0.46	0.12	2.2	0.07	40.8	1.7	1.85	29.9	9.0
F6	New Pool next ppt.s	0.32	0.25	9.5	0.26	31.2	7.0	1.85	5.40	9.9
F7	GPS Upper filtrate	0.83	0.20	17.1	5.88	0.06	306	1.71	0.0057	12.1
F8	GPS spring	0.14	0.07	37.5	6.96	0.07	345	1.60	0.0026	12.1
F9	Wedding Cake seep	0.02	0.06	58.1	0.52	0.35	136	0.97	0.0099	11.4
F10	Pool G	0.50	0.26	39.3	1.27	0.19	57	3.0	0.0081	11.6
F11	Pool C	0.24	0.14	41.8	1.26	0.20	56	3.1	0.0079	11.6
F12	Blue Pool	0.12	0.07	51.0	1.27	0.18	57	3.3	0.0057	11.65
F13	BSC2 10/16	0.16	0.12	54.0	1.26	0.098	56	3.5	0.0030	11.7
F14	Pool E	0.27	0.21	41.7	1.57	0.198	57	3.1	0.0078	11.6
F15	Wedding Cake 9/16	0.14	0.11	47.8	0.76	9.8	20	3.5	0.338	11.3
4/14	Creek above Barnes Cpx	——		1.2†	0.06	49.0	1.6	1.37	66.0	7.8
8/16	Creek above Barnes Cpx	——		3.1†	0.10	40.9	4.0	1.83	21.8	8.7
8/13	Creek below Camp	——		8.0†	0.67	41.1	39	2.17	8.52	9.5

* Ca concentrations by isotope dilution except those marked † that were conducted by Q-ICPMS. Other element concentrations by Q-ICPMS, pH measured in the field.

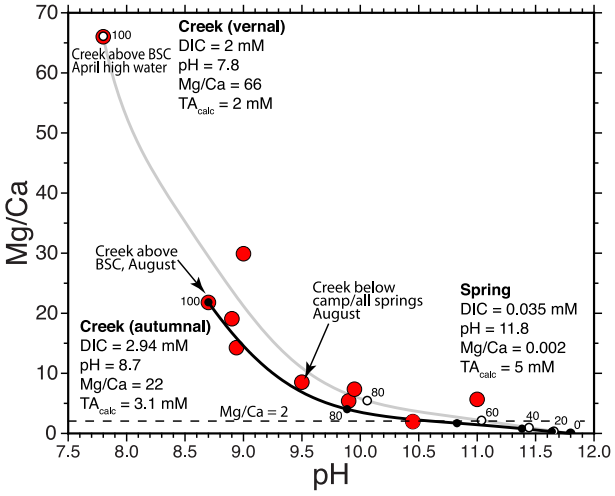

Fig. 6. Mixing model between creek and spring waters showing pH vs. Mg/Ca molar ratio. Curves model mixing between BSC Spring water (pH = 11.8, Mg/Ca = 0.002) and Austin Creek water (April at high-flow, upper grey curve, pH = 8.7, Mg/Ca = 66; August near low-flow, lower black curve, pH = 8.7; Mg/Ca = 22). The dashed horizontal line indicates a Mg/Ca ratio of 2.

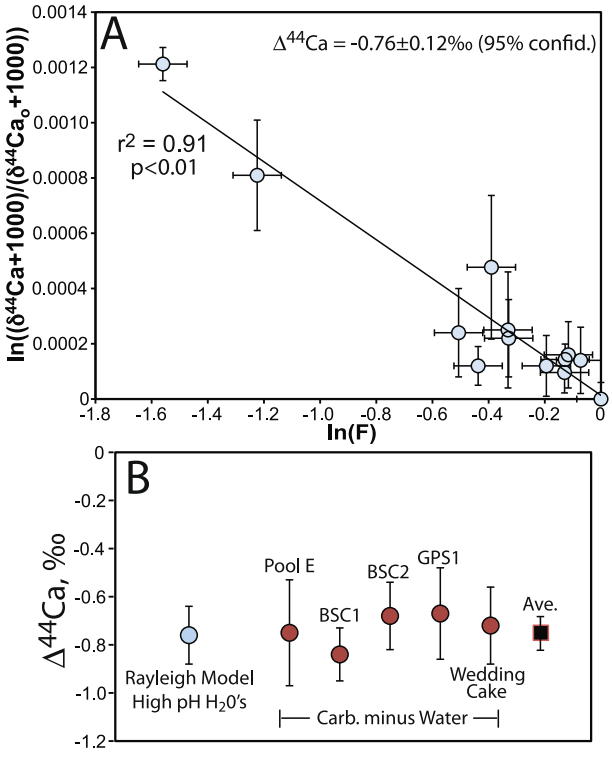

Fig. 7. **(A)** δ^{44}Ca Rayleigh fractionation model plot for high-pH waters (>11.0) from The Cedars springs and pools. The value of F (the fraction of Ca remaining) is based on the water sample with the highest Ca concentration (58 ppm) and lowest δ^{44}Ca (0.02 ± 0.06) from the seep above the Wedding Cake Pool (sample F9). The slope of the best-fit line gives a calcium isotope fractionation factor (Δ^{44}Ca) of −0.76 ± 0.12‰ (2σ). **(B)** Summary of Δ^{44}Ca determined from $CaCO_3$-water pairs (red circles) and the Rayleigh model shown in A for waters with pH ≥ 11.0.

−0.75 ± 0.07‰, in good agreement with the value from the Rayleigh distillation calculation (Fig. 7B).

4.5. $\delta^{18}O$ and $\delta^{13}C$ of calcium carbonate samples

Calcium carbonate $\delta^{18}O$ and $\delta^{13}C$ data are presented in Table 3 and Tables S1–S3, and displayed in Fig. 8 along with data for calcium carbonates from The Cedars analyzed by Meister et al. (2011). The $\delta^{18}O$ and $\delta^{13}C$ values of the carbonates of all textures fall along a roughly 1:1 line, far from the expected composition for calcium carbonate in

Table 3
Ca, C, and O isotopic compositions of calcium carbonates.

Label	Description	$\delta^{44}Ca_{BSE}$, ‰	±2σ	$\delta^{13}C_{VPDB}$, ‰	$\delta^{18}O_{VPDB}$, ‰
Carb A	Wedding Cake rim (4/5/14)	−0.46	0.09	−14.62	−4.24
Carb B	New Pool xtl strings #1 (10/11/14)	−0.17	0.07	−11.78	−3.76
Carb C	New Pool encrustation (10/11/14)	−0.46	0.10	−12.00	−3.65
Carb D	BSC floe, upstream (10/11/14)	−0.77	0.11	−26.48	−19.06
Carb E	BSC floe, middle (10/11/14)	−0.69	0.08	−26.73	−18.32
Carb F	BSC floe, downstream (10/11/14)	−0.52	0.19	−26.66	−18.79
Carb G	New Pool xtl strings #2 (10/11/14)	−0.42	0.11	−12.34	−4.80
Carb H	GPS floe (10/11/14)	−0.38	0.02	−21.39	−13.47
Carb I	BSC large floe sample (10/11/14)	−0.66	0.06	−26.71	−18.71
Carb J	GPS upper filtered carb (10/11/14)	−0.68	0.04	−13.48	−0.36
Carb K	GPS filtered carb (10/11/14)	−0.65	0.07	−13.54	−5.13
Carb L	GPS floe (8/3/13)	−0.41	0.10	−23.04	−14.74
Carb M	Wedding Cake 1 cm below rim (10/11/14)	–	–	−14.29	−3.56
Carb N	Wedding Cake 15 cm below rim (10/11/14)	–	–	−15.08	−4.58
Carb P	Pool E floe (PE-C1) (10/7/16)	−0.48	0.07	−27.55	−19.58
Carb Q	Wedding Cake Floe (9/2/16)	−0.58	0.11	−17.45	−6.69
Carb R	BSC2 Floe (10/7/16)	−0.52	0.07	−25.50	−18.77

Table 4
Calculated values of Ca isotopic fractionation due to carbonate precipitation using data from Tables 2 and 3 for floe/water pairs.

Observation	$\Delta^{44/40}$Ca, ‰, ±2σ
Rayleigh model with all high pH waters	−0.76 ± 0.12
Wedding Cake (Carb Q – F15)	−0.72 ± 0.16
BSC1 (Avg. of Carbs D,E,F, & I minus F4)	−0.84 ± 0.11
BSC2 (Carb R-F13)	−0.68 ± 0.14
BSC Pool E (Carb P-F14)	−0.75 ± 0.22
GPS1 (Carb L-F1)	−0.67 ± 0.19
Weighted Average $CaCO_3$-Water	−0.75 ± 0.07
Weighted Average all values	−0.75 ± 0.06

equilibrium with Cedars water ($\delta^{18}O \sim -6$‰ VPDB). This 1:1 array stretches from highly fractionated, low values of $\delta^{13}C$ and $\delta^{18}O$ toward, but not reaching, the composition of atmospheric CO_2. The carbonate samples with the lowest $\delta^{18}O$ and $\delta^{13}C$ values are floes from BSC. Other floe samples from GPS fall further up the array, while a floe sample from the Wedding Cake pool is near the high end of the array. Calcium carbonate of different occurrences (textures), pool rim material, and snow from pool bottoms, have compositions distributed along the 1:1 array. The samples from the Wedding Cake (floe and rim materials) are displaced to the left of the main array, while samples of old laminated carbonates (travertine) form a separate parallel array displaced to the right. Samples of snow from a GPS pool (Carb J, Table 2; GPS-1 #1-3, Table S1) have the highest $\delta^{18}O$ of all calcium carbonate samples.

5. DISCUSSION

5.1. Floe growth rate

The sample of floe material collected after eight days of growth (Fig. 5) had a thickness of ~20 μm and provides a constraint on the growth rate of calcium carbonate precipitation represented by floe formation on pool surfaces. The rate of caclium carbonate growth per square meter is provided by Eq. (1):

$$R(\mathrm{mol/m^2/s}) = (d \cdot \rho)/(M \cdot t) \quad (1)$$

where d is the floe thickness (meters), ρ is the floe density (g/m^3) taking into account porosity and the proportions of calcite and aragonite, M is the molecular weight of $CaCO_3$ (100.086 g/mole), and t is the time interval of growth (seconds). Given a thickness of ~20 μm, a growth time of eight days, a porosity of 0 to 40% (Fig. 4), and a mineral composition of 80% calcite and 20% aragonite, Eq. (1) yields a growth rate range of 4.8×10^{-7} mol/m^2/s to 8.0×10^{-7} mol/m^2/s. From this range in growth rate, an estimate can be made of the aragonite saturation state (Ω) through the equation $R = k(\Omega - 1)^n$ where the rate constant k is given for aragonite precipitation by the empirical relation $\ln(k) = 11.54 - 8690/T$ (T in Kelvin) and the reaction order, n, is 1.7 (Romanek et al. 2011). Applying this equation to the growth rate range at T = 17.4°C yields a Ω of ~ 9–13. This compares well with the Ω estimates made by Morrill et al. (2013) of ~13 for BSC (where our growth rate was measured) and ~ 5 for GPS based on measured ion chemistry.

The calculated range in aragonite growth rate, along with the average $\Delta^{44/40}$Ca value of −0.75 ± 0.07‰ derived above is plotted in Fig. 9 for comparison to synthetic calcite (Tang et al., 2008; Watkins et al., 2017), calcitic travertine (Yan et al., 2016), and theoretical values based on the DePaolo (2011) surface reaction kinetic model for calcite. The result for The Cedars falls along the upper bound of the array of experimental data, suggesting that the growth rate-dependence is fairly consistent across a broad range of pH values.

The inferred growth rate for floe carbonate has implications for the rate of spring resupply to pools, in particular the main BSC pool. For a Ca concentration of 51.7 ppm in the spring water supply of the pool, the growth of each square centimeter of floe to a thickness of 25 μm would require between 43 and 53 ml (depending on density/porosity of the floe) of BSC spring water. The pool water

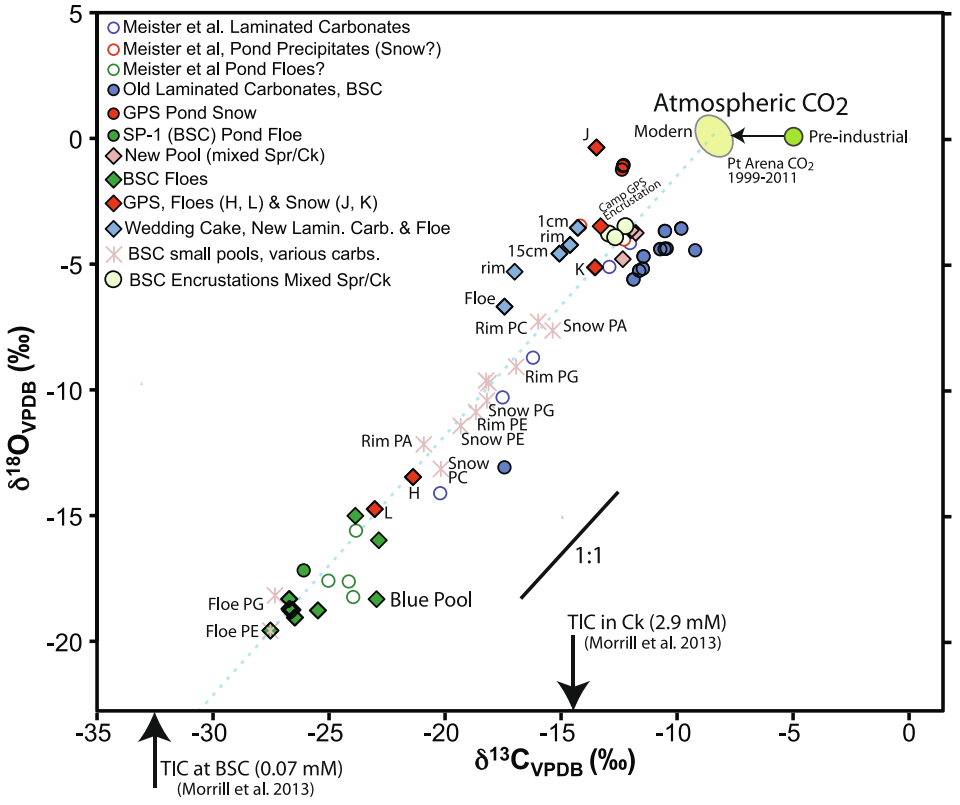

Fig. 8. The carbon and oxygen isotopic compositions of carbonate samples from The Cedars. Open circles show data from Meister et al. (2011). Vertical arrows along the x-axis show the $\delta^{13}C$ of total inorganic carbon (TIC) from a pool sample at the BSC, and TIC for a sample of Austin Creek (Morrill et al., 2013). Shown for reference is the isotopic composition of atmospheric CO_2 (Pt Arena, CA data from White et al., 2015) and an estimate for pre-industrial atmospheric CO_2. The black line shows the slope of a 1 to 1 correlation between $\delta^{18}O$ and $\delta^{13}C$, which is parallel to the blue dashed line provided for visual reference.

beneath floes represented by samples D, E, F and I had a calcium concentration of 51.1 ppm that is indistinguishable from the BSC spring sample taken at that time (51.7 ppm). Given the area of the pool (roughly 1.6 m^2), a supply rate of fresh spring water to the pool of ~1 ml/s (or ~85 L/day) would be required in order to maintain both the Ca concentration and Ca isotope composition. At the Wedding Cake pool, the supply of fresh spring water can be limited relative to carbonate precipitation, since at times the Ca concentration can be driven down by a factor of ~5 relative to the spring source, and the Ca isotope composition of the pool can be fractionated (fluid F3 $\delta^{44}Ca = 1.23‰$) by calcium carbonate precipitation.

The calcium carbonate growth rate inferred above is comparable to the expected flux of CO_2 from the atmosphere to the pool water. In a set of $BaCO_3$ precipitation experiments at pH = 10 using a hydroxide buffer, Usdowski and Hoefs (1986) measured a CO_2 flux of 4.7×10^{-7} mol/m^2/s, which compared well to their own calculated estimate based on CO_2 diffusivity in water and the $CO_{2(aq)}$ hydroxylation rate constant. The similarity between this value at pH 10 and our growth rate estimates for samples precipitated at pH > 10 suggests that calcium carbonate floe growth and uptake of atmospheric CO_2 are strongly coupled (see Section 5.3).

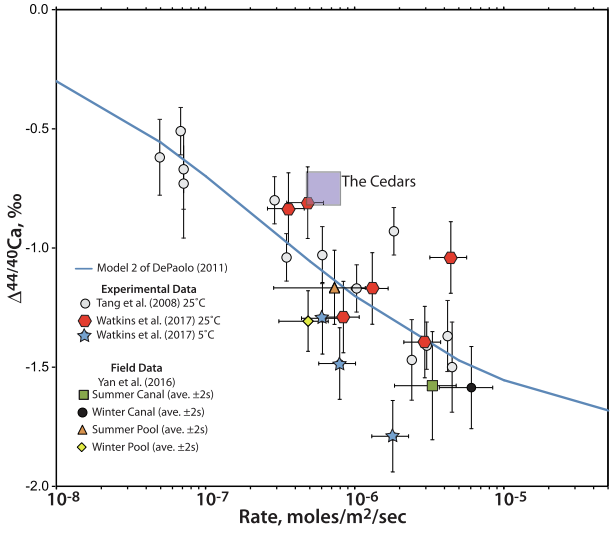

Fig. 9. Comparison of $\Delta^{44}Ca$ vs crystal growth rate data between aragonite/calcite floes at The Cedars (this study), synthetic calcite (Tang et al., 2008; Watkins et al., 2017), modern calcitic travertine (Yan et al., 2016) and the DePaolo (2011) surface kinetic model for calcite. Error bars represent ±2σ intervals of the reported values.

5.2. Aragonite precipitation

We observed aragonite in all of our samples examined with XRPD or SEM, as did Meister et al. (2011) and O'Neil and Barnes (1971), including in pool rims, pool snow, pool floes and precipitates from mixed spring/creek waters (Table 1, Figs. 4 and 5, Figs. S1–S4). Meister et al. (2011) propose that aragonite at The Cedars is associated with high Mg/Ca molar ratios of the water resulting from mixing of high Mg/Ca ratio creek water with the low Mg/Ca spring water leading to a high enough Mg/Ca ratio to inhibit the precipitation of calcite in favor of metastable aragonite. Several direct observations argue against high Mg/Ca as the explanation for all occurrences of aragonite at The Cedars. The pools at the BSC produce floes of aragonite/calcite from solutions with very low Mg/Ca ratios (<0.01, see above and Table 2), with aragonite as the first phase to precipitate followed by calcite (Fig. 4). Likewise, the rims and snow of low Mg/Ca spring pools also contain aragonite. The high pH of spring pools is sensitive to additions of creek water with a pH of 7.8–8.7. Mixing models demonstrate that even with the addition of creek water with Mg/Ca = 21.8, the Mg/Ca of the mixture does not rise above 2 until the pH falls well below 11 (Fig. 6). Such pH values are not seen in the spring pools (pH range 11.3–12.0, Table 2). However, there are instances of aragonite occurring at locations where spring water enters the creek directly (e.g. Carb B and Carb C, see Suppl. Fig S2 and S3) where high Mg/Ca may play a role in favoring aragonite over calcite. Such samples, precipitating from clearly mixed spring/creek water (Carbs B and C in Table 3; Carbs S, T, Y and AA in Table S1; Samples labeled "mixed Spr/Cr" in Fig. 7), have C and O isotope compositions distinct from aragonite/calcite samples precipitated from spring water.

Alternative chemical variables that potentially can promote aragonite precipitation over calcite from cool springs include high pH and the degree of oversaturation (see review by Jones, 2017). Experiments by Tai and Chen (1998) demonstrate that the favored calcium carbonate polymorph is a function of solution pH. They found at 24 °C that with pH below 10–10.5, vaterite is the favored polymorph to crystallize, while at pH ≥ 12–11.8 calcite is dominant, and for pH in the range of 10.5–11.5 aragonite was the dominant polymorph peaking in abundance at pH ~ 11.3. Similar effects of pH on carbonate polymorphism were found by Matsumoto et al. (2010). The degree of supersaturation has been shown by Kawano et al. (2009) to control polymorphism, with high ($\Omega > 15$ at 20 °C) saturation favoring vaterite and at $\Omega < 15$ favoring calcite. However, these experiments were likely conducted at circum-neutral pH (the pH conditions were measured but not given by Kawano et al., 2009) and so may be consistent with the experiments of Tai and Chen (1998) in which at a Ω of ~40 and pH < 10 vaterite precipitation was favored.

From the SEM observations of floes discussed above, the first phase to precipitate is aragonite, followed by calcite. This is consistent with the surface layer of the water having a pH of 11.0–11.5 and a Ω of 9–13 favoring the nucleation of aragonite over calcite. As the layer thickens it encounters a pH > 11.5 and calcite begins to nucleate and grow. In considering the preferred nucleation of aragonite in modern seawater, Sun et al. (2015) conclude based on *ab initio* calculations that aragonite is favored over calcite for Mg/Ca ratios in the solution greater than ~2 due to Mg incorporation stabilizing aragonite relative to calcite. We speculate that the effect of pH is to change the surface energy of calcium carbonate nuclei such that the aragonite nucleation rate is maximized at pH 11.0–11.5, whereas calcite nucleation and growth is promoted at higher pH.

5.3. Modeling of kinetic oxygen and carbon isotope fractionation

A significant advance of the past decade has been the development of quantitative models of kinetic isotope effects between precipitating calcium carbonate crystals and dissolved ions (DePaolo, 2011; Nielsen et al., 2012, 2013; Watkins et al., 2013, 2014, 2017; Devriendt et al., 2017) and between DIC species and water (Devriendt et al., 2017; Chen et al., 2018). Chen et al (2018) developed a model for oxygen and carbon isotopes that integrates reaction kinetics of the DIC species, carbonate precipitation and fluid mixing - a combination that is necessary to understand alkaline springs like those at The Cedars. This model is informed by extensive experimental and theoretical work on the kinetics and isotope fractionations among DIC species (e.g. Usdowski et al., 1991; Clark et al., 1992; Usdowski and Hoefs, 1993; Zeebe and Wolf-Gladrow, 2001; Beck et al., 2005; Kim et al., 2006; Zeebe, 2014; Sade and Halevy, 2017, 2018) and carbonate minerals (Romanek et al., 1992; Kim et al., 2007; Wolthers et al., 2012; Watkins et al., 2013, 2014). In this section, we present a model adapted from that of Chen et al. (2018), with addition of diffusive effects at the atmosphere-water interface and use it to evaluate the observed C and O isotope variations, while also using the constraints we have on carbonate growth rates and Ca isotope compositions.

We begin with a conceptual model (Fig. 10) of the precipitation of surface floes for which we have observational constraints. The floe initiates growth with various nucleation events at the water–air interface as CO_2 is absorbed from the atmosphere and dissolved into the water (O'Neil and Barnes, 1971; Meister et al. 2011), where it undergoes hydroxylation to form HCO_3^- with subsequent rapid and near-quantitative conversion to CO_3^{2-}. The precipitation of calcium carbonate to build the floes consumes much of the DIC coming from the atmosphere. The isotopic composition of the DIC (essentially all in the form of CO_3^{2-}) is set by hydroxylation of the incoming atmospheric CO_2 to extremely low $\delta^{13}C$ and $\delta^{18}O$ values, and remains at such values unless shifted by the addition of DIC from spring or creek water.

As the floe thickens, it eventually detaches and sinks, carrying with it some of the surface water (with DIC having low $\delta^{13}C$ and $\delta^{18}O$) into the deeper pool. Hence, the deeper pool water from which the "snow" and rim carbonates precipitate obtains some of its DIC from the boundary layer near the surface either by diffusion or by the fluid boundary layer physically detaching, sinking, and mixing with the deep water. Isotopic equilibration of the detached layer is

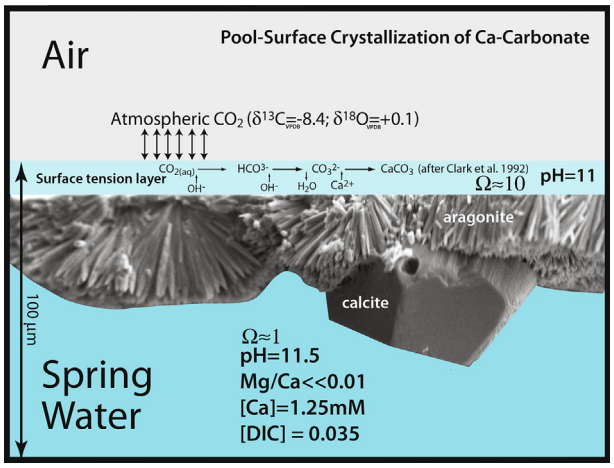

Fig. 10. Conceptual model for the evolution of calcium carbonate floes at the surface of high pH waters. Within the water surface layer (not shown to scale) aragonite nucleation/growth rates are greater than those of calcite, consistent with ~pH = 11 (Tai and Chen 1998). As the aragonite layer thickens down into the water below with pH ≥ 11.5 calcite nucleation/growth rates become greater than aragonite (Tai and Chen 1998) resulting in overgrowth by calcite rhombs. Through disturbance of the pool's surface due to wind, falling debris, rain, etc. the surface tension is broken and the floe sinks to the bottom where continued calcite precipitation can occur. With the surface cleared, the process of floe formation begins again.

hindered by the high pH of the pool water, so the kinetic signature of the surface processes can be preserved for a long period of time—days to tens of days at pH = 11.5 (Usdowski et al., 1991).

This conceptual framework is used to construct a two-stage model for what is happening at The Cedars (Fig. 11). The first stage, hereafter referred to as the thin-film model, focuses on the diffusional boundary layer (~100 µm) at the pool-atmosphere interface. We solve a system of reaction–diffusion equations to compute the concentrations and isotopic compositions of DIC species throughout the one-dimensional model domain. The results place constraints on the hydroxylation kinetic fractionation factors (KFF = (α-1)·1000), which are used for defining the isotopic composition of the equilibrated inorganic carbon (EIC = HCO_3^- + CO_3^{2-}; Chen et al., 2018) flux in the second stage. The second stage, hereafter referred to as the box model, describes the isotopic composition of a well-mixed reservoir as a function of the following fluxes with distinct isotopic compositions: (1) an EIC flux from the detached surface layer, (2) a spring replenishment flux, (3) a low-pH (8.7) creek flux, and (4) a $CaCO_3$ precipitation flux. The box model also includes reactions among DIC species. The results are used to determine the environmental conditions required to produce the full $\delta^{18}O$-$\delta^{13}C$ data array.

5.3.1. Thin-film model

For the thin-film model, we start with a pool having a pH of 11.5 and a low DIC concentration of ~0.035 mM, based on the value for a BSC water sample given by Morrill et al. (2013). With these specified pH and DIC values, all other carbonate parameters are calculated based on expressions given by Zeebe and Wolf-Gladrow (2001) and pK values from Millero et al. (2007). The pool is assumed to be isotopically equilibrated initially (Table 5) and at saturation with respect to calcite ($\Omega = 1$), from which we calculate an initial Ca^{2+} concentration of 1.3 mM, in the range of 0.94 to 1.3 mM reported by Morrill et al. (2013).

The rate of CO_2 uptake from the atmosphere is determined by the contrast between the partial pressure (or fugacity) of the atmospheric CO_2 and the concentration of $CO_{2(aq)}$ in the surface water of the pool. The exchange across the surface between the gas phase CO_2 and the water is assumed to be very fast in comparison to the diffusive transport of the CO_2 into the pool away from the surface; i.e., local equilibrium:

$$[CO_2]_{interface} = K_0 \cdot f_{CO2}, \quad (2)$$

where K_0 is Henry's constant (mol/kg-soln/atm) and f_{CO2} is the fugacity of CO_2 (atm). For a 400 ppm atmosphere, this leads to $[CO_2]_{eq} = 1.6 \times 10^{-5}$ moles/kg-soln which is several orders of magnitude higher than the concentration in the bulk pool. The incoming CO_2 is converted to HCO_3^- according to the following reactions (Chen et al. 2018):

$$CO_2 + H_2O \underset{k_{-1}}{\overset{k_{+1}}{\rightleftarrows}} HCO_3^- + H^+ \quad \text{(Reaction 1)}$$

$$CO_2 + OH^- \underset{k_{-4}}{\overset{k_{+4}}{\rightleftarrows}} HCO_3^- \quad \text{(Reaction 2)}$$

$$^{13}CO_2 + H_2O \underset{k'_{-1}}{\overset{k'_{+1}}{\rightleftarrows}} H^{13}CO_3^- + H^+ \quad \text{(Reaction 3)}$$

$$^{13}CO_2 + OH^- \underset{k'_{-4}}{\overset{k'_{+4}}{\rightleftarrows}} H^{13}CO_3^- \quad \text{(Reaction 4)}$$

$$CO_2 + H_2{}^{18}O \underset{1/3a_{-1}}{\overset{a_{+1}}{\rightleftarrows}} HC^{18}OO_2^- + H^+ \quad \text{(Reaction 5)}$$

$$CO_2 + {}^{18}OH^- \underset{1/3a_{-4}}{\overset{a_{+4}}{\rightleftarrows}} HC^{18}OO_2^- \quad \text{(Reaction 6)}$$

$$C^{18}OO + H_2O \underset{2/3b_{-1}}{\overset{b_{+1}}{\rightleftarrows}} HC^{18}OO_2^- + H^+ \quad \text{(Reaction 7)}$$

$$C^{18}OO + OH^- \underset{2/3b_{-4}}{\overset{b_{+4}}{\rightleftarrows}} HC^{18}OO_2^- \quad \text{(Reaction 8)}$$

Rate constants for the ^{18}O substituted species are represented by a for substitution on H_2O or OH^-, and represented by b for substitution on CO_2. The factors of 1/3 and 2/3 (reactions 5 to 8) are necessary for oxygen isotope mass balance. For every mole of $HC^{18}OO_2^-$ that undergoes dehydration, 2/3 goes to $C^{18}OO$ and 1/3 goes to $H_2^{18}O$. Hence, the rate of change of $H_2^{18}O$ is proportional to 1/3 of the concentration of $HC^{18}OO_2^-$. A similar argument can be made for the (de-)hydroxylation reactions involving

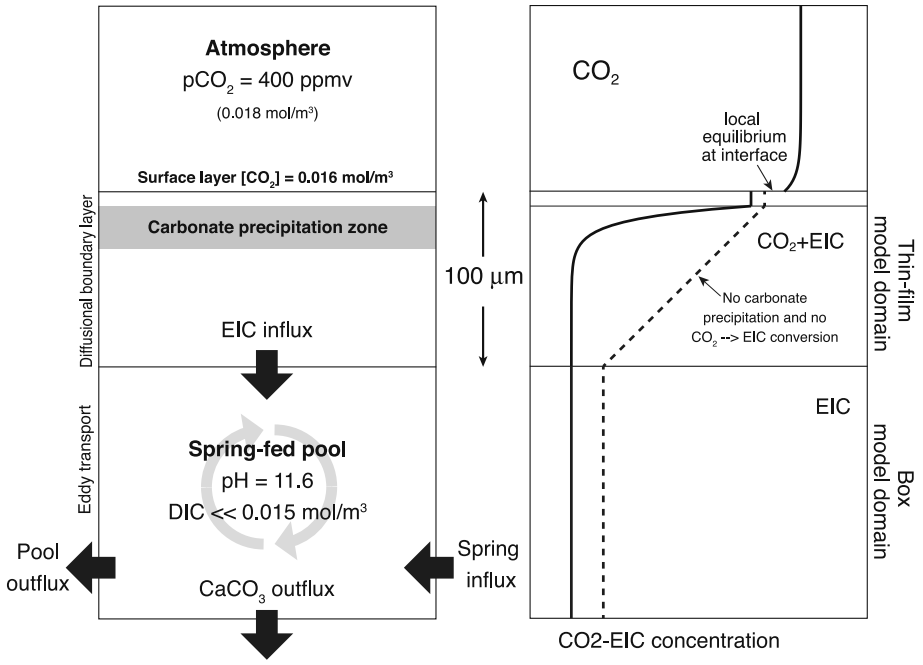

Fig. 11. Schematic diagram showing how the two stages of the isotopic model fit together. The thin-film model focuses on processes within the 100 µm diffusional boundary layer at the pool-atmosphere interface and tracks spatial variations in DIC species' concentrations and isotopic compositions. The box model focuses on the larger scale of the bulk pools and how the DIC species' concentrations and isotopic compositions vary as a function of three fluxes: (1) DIC from the thin film, (2) DIC replenishment from the spring water inflow and outflow, and (3) $CaCO_3$ precipitation.

Table 5
Compilation of equilibrium fractionation factors (EFFs; T in Kelvin unless otherwise noted).

Compounds	Equation	α (17.4 °C)	Reference
Carbon isotopes			
$CO_{2(g)}$ - HCO_3^-	$-9.483\ T^{-1} + 1.02389$	0.9913	Mook (1986)
$CO_{2(aq)}$ - HCO_3^-	$-9.866\ T^{-1} + 1.02412$	0.9902	Mook (1986)
CO_3^{2-}-HCO_3^-	$-0.867\ T^{-1} + 1.00252$	0.9995	Mook (1986)
$CO_{2(g)}$-Calcite	$\exp\left(\frac{-2.4612+\frac{7666.3}{T}-\frac{2988000}{T^2}}{1000}\right)$	0.9886	Bottinga (1968)
Oxygen isotopes			
$CO_{2(aq)}$ – H_2O	$\exp(2520\ T^{-2} + 0.01212)$	1.0429	Beck et al. (2005)
HCO_3^-- H_2O	$\exp(2590\ T^{-2} + 0.00189)$	1.0331	Beck et al. (2005)
CO_3^{2-}- H_2O	$\exp(2390\ T^{-2} - 0.00270)$	1.0259	Beck et al. (2005)
Calcite – H_2O	$\exp\left(\frac{17747}{T}-29.777\right)$	1.0318	Coplen (2007), Watkins et al. (2013)
OH^- - H_2O	$(1 + [23.5 - 0.0728(T_C\text{-}25)] / 1000)^{-1}$	0.9765	Zeebe (2020)
	or		
OH^- - H_2O	$(1 + [19.1 - 0.0455(T_C\text{-}25)] / 1000)^{-1}$	0.9809	Zeebe (2020)

$HC^{18}OO_2^-$. The ratios of forward to backward rate constants are equal to the equilibrium constant for each reaction, as given in Table 6.

At high pH (>11), CO_2 hydroxylation is much faster than CO_2 hydration because of the high OH^- concentration. We nevertheless retain the hydration reactions for completeness. The increase in CO_2 and HCO_3^- at the surface establishes large concentration gradients that drive diffusion of DIC species downward through the thin film. At the base of the thin film (z = −100 µm), we assume the pool is well-mixed and able to maintain fixed concentrations of dissolved species. For simplicity we assume that all dissolved species diffuse at the same rate and that there is no isotopic fractionation by diffusion (Zeebe, 2011).

Table 6
Constants and parameters used in the model.

Symbol	Meaning	Value	Reference/Note
Part I: Fluxes and elementental concentrations			
F_{spr}	Spring mass flux	0.001 kg-sol/s	To maintain $[Ca^{2+}]$, see text
$[DIC]_{spr}$	Spring [DIC]	0.035 mM	Morrill et al. (2013)
$[Ca^{2+}]_{spr}$	Spring $[Ca^{2+}]$	1.3 mM	Morrill et al. (2013)
$[Alk]_{spr}$	Spring total alkalinity	2.6 mM	Calc. from DIC & pH
$[CO_2]_{spr}$	Spring $[CO_2]_{(aq)}$	1.0×10^{-8} mM	Calc. from DIC & pH
$[EIC]_{spr}$	Spring $[HCO_3^-] + [CO_3^{2-}]$	0.035 mM	Calc. from DIC & pH
F_{cr}	Creek mass flux	Variable (kg-soln/s)	-
$[DIC]_{cr}$	Creek [DIC]	2.9 mM	Morrill et al. (2013)
$[Ca^{2+}]_{cr}$	Creek $[Ca^{2+}]$	0.13 mM	Morrill et al. (2013)
$[Alk]_{cr}$	Creek total alkalinity	3.0 mM	Calc. from DIC & pH
$[CO_2]_{cr}$	Creek $[CO_2]_{(aq)}$	0.011 mM	Calc. from DIC & pH
$[EIC]_{cr}$	Creek $[HCO_3^-] + [CO_3^{2-}]$	2.89 mM	Calc. from DIC & pH
J_{atm}	EIC flux through thin water film	6×10^{-7} moles/m^2/s	Usdowski & Hoefs (1986)
SA_{pool}	Surface area of pool	1 m^2	-
J_{CaCO3}	Carbonate precipitation rate (moles/m^2/s)	$J_{CaCO3} = k_{rate}(\Omega\text{-}1)^{1.7}$	Romanek et al. (2011)
		$\ln k_{rate} = 11.54\text{-}(8690/T_K)$	Romanek et al. (2011)
		$\Omega = \frac{[Ca^{2+}][CO_3^{2-}]}{K_{sp}}$	Definition
Sp	Reactive surface area (m^2/kg-soln)	Adjustable parameter	0.01 to 1000
F^*_{spr}	Spring DIC flux (moles/s)	$F^*_{spr} = F_{spr} \cdot [DIC]_{spr}$	-
F^*_{cr}	Creek DIC flux (moles/s)	$F^*_{cr} = F_{cr} \cdot [DIC]_{cr}$	-
F^*_{atm}	Atmospheric DIC flux (moles/s)	$F^*_{atm} = J_{atm} \cdot SA_{pool}$	-
Part II: Reaction rate constants			
χ	Fraction of HCO_3^- in EIC	$\chi = \left(1 + \frac{K_2}{[H^+]}\right)^{-1}$	K_2 from Millero et al. (2007)
k_{+1}	Rate const. CO_2 hydration (s^{-1})	$\log_{10}k_{+1} = 329.85 - 110.54\log_{10}(T_K) - \frac{17265.4}{T_K}$	Pinsent et al. (1956)
k_{-1}	Rate const. CO_2 dehydration (M^{-1}s^{-1})	$k_{-1} = k_{+1}/K_1$	K_1 from Millero et al. (2007)
k_{+4}	Rate const. CO_2 hydroxylation (M^{-1}s^{-1})	$\log_{10}k_{+4} = 13.635 - \frac{2895}{T_K}$	Pinsent et al. (1956)
k_{-4}	Rate const. CO_2 dehydroxylation (s^{-1})	$k_{-4} = k_{+4} \cdot (K_w/K_1)$	K_w from DOE (1994)
Part III: Isotopic parameters			
r_w	$^{18}O/^{16}O$ ratio of H_2O	0.00199377	$\delta^{18}O_{VSMOW} = -5.7‰$
$r_{CO2(g) \text{ or } (aq)}$	$^{18}O/^{16}O$ ratio of CO_2	-	Isotope ratio
r_{EIC}	$^{18}O/^{16}O$ ratio of EIC	-	Isotope ratio
$R_{CO2(g) \text{ or } (aq)}$	$[C^{18}OO]/[CO_2]$	$2r_{CO2}$	Isotopologue ratio
R_{EIC}	$[^{18}EIC]/[^{16}EIC]$	$3r_{EIC}$	Isotopologue ratio
$^{13}\chi$	Fraction of $H^{13}CO_3^-$ in ^{13}EIC	$^{13}\chi = \left(1 + \frac{K_2 \cdot {}^{13}\alpha_{CO_3^{2-}/HCO_3^-}}{[H^+]}\right)^{-1}$	-
$^{18}\chi$	Fraction of $HC^{18}OOO^-$ in ^{18}EIC	$^{18}\chi = \left(1 + \frac{K_2 \cdot {}^{18}\alpha_{CO_3^{2-}/HCO_3^-}}{[H^+]}\right)^{-1}$	-
k'_{+1}	Rate const. for $^{13}CO_2$ hydration (s^{-1})	$k'_{+1}/k_{+1} = 0.987$	Zeebe and Wolf-Gladrow (2001)
k'_{-1}	Rate const. for $^{13}CO_2$ dehydration (M^{-1}s^{-1})	$k'_{+1}/k'_{-1} = K_1 \cdot {}^{13}\alpha_{HCO_3^-/CO_{2(aq)}}$	Equilibrium constraint
k'_{+4}	Rate const. for $^{13}CO_2$ hydrox. (M^{-1}s^{-1})	$k'_{+4}/k_{+4} = 0.9829$	This study
k'_{-4}	Rate const. for $^{13}CO_2$ dehydrox. (s^{-1})	$k'_{+4}/k'_{-4} = K_1/K_w \cdot {}^{13}\alpha_{HCO_3^-/CO_{2(aq)}}$	Equilibrium constraint

a_{+1}, b_{+1}	Rate const. for CO_2 hydration (s^{-1})	$a_{+1}/k_{+1} = 1.0000$ $b_{+1}/k_{+1} = 0.9812$	Yumol et al. (2020)†
a_{-1}, b_{-1}	Rate const. for CO_2 dehydration ($M^{-1}s^{-1}$)	$a_{+1}/a_{-1} = K_1 \cdot \alpha_{HCO_3^-/H_2O}$ $b_{+1}/b_{-1} = K_1 \cdot \alpha_{HCO_3^-/CO_2}$	Equilibrium constraint Equilibrium constraint
a_{+4}, b_{+4}	Rate const. for CO_2 hydrox. ($M^{-1}s^{-1}$)	$a_{+4}/k_{+4} = 0.9988$ $b_{+4}/k_{+4} = 1.0000$	This study‡ This study‡
a_{-4}, b_{-4}	Rate const. for CO_2 dehydrox. (s^{-1})	$a_{+4}/a_{-4} = \frac{K_1}{K_w} \cdot \frac{1}{\alpha_{OH^-/H_2O}}$ $b_{+4}/b_{-4} = \frac{K_1}{K_w} \cdot \alpha_{HCO_3^-/CO_2}$	Equilibrium constraint Equilibrium constraint
$^{13}R_{EIC(hydrox)}$	Composition of hydroxylated CO_2	18.1‰ lighter than $CO_{2(atm)}$	This study
$^{18}R_{EIC(hydrox)}$	Composition of hydroxylated CO_2	7.1‰ lighter than 'CO_2+H_2O'	This study
E_C	Calcite- CO_3^{2-} equilibration index	$E_C = \Omega^{-n_2}$, where $n_2 = 0.2$	Devriendt et al. (2017)
$^{13}\alpha_{CaCO_3/CO_3^{2-}}$	Growth rate-dependent isotopic fractionation	$\frac{1+E_C\left(^{13}\alpha_f/^{13}\alpha_{eq}-1\right)}{^{13}\alpha_f}$, $^{13}\alpha_f = 1.0000$ and $^{13}\alpha_{eq} = 1.0032$	DePaolo (2011) Watkins and Hunt (2015)
$^{18}\alpha_{CaCO_3/CO_3^{2-}}$	Growth rate-dependent isotopic fractionation	$\frac{1+E_C\left(^{18}\alpha_f/^{18}\alpha_{eq}-1\right)}{^{18}\alpha_f}$, $^{18}\alpha_f = 0.9995$ and $^{18}\alpha_{eq} = 1.0057$	DePaolo (2011) Devriendt et al. (2017)
$^{13}\alpha_{CaCO_3/EIC}$	Growth rate-dependent isotopic fractionation	$^{13}\alpha_{CaCO_3/CO_3^{2-}} \cdot \left(1 - {}^{13}\chi\right)/(1-\chi)$	- -
$^{18}\alpha_{CaCO_3/EIC}$	Growth rate-dependent isotopic fractionation	$^{18}\alpha_{CaCO_3/CO_3^{2-}} \cdot \left(1 - {}^{18}\chi\right)/(1-\chi)$	- -

† These values yield a bulk KFF consistent with Yumol et al. (2020)
‡ These values yield a bulk KFF consistent with 'this study' in Table 7.

The combined process of reaction and diffusion is modeled by solving the following system of partial differential equations:

$$\frac{\partial[CO_2]}{\partial t} = D_{CO_2} \cdot \frac{\partial^2[CO_2]}{\partial z^2} + \{-k_{+1}[CO_2] + k_{-1}[EIC] \cdot \chi \cdot [H^+] - k_{+4}[CO_2][OH^-] + k_{-4}[EIC] \cdot \chi\} \quad (3)$$

$$\frac{\partial[EIC]}{\partial t} = D_{EIC} \cdot \frac{\partial^2[EIC]}{\partial z^2} + \{k_{+1}[CO_2] - k_{-1}[EIC] \cdot \chi \cdot [H^+] + k_{+4}[CO_2][OH^-] - k_{-4}[EIC] \cdot \chi\} - Sp \cdot J_{CaCO_3} \quad (4)$$

$$\frac{\partial[Ca^{2+}]}{\partial t} = D_{Ca} \cdot \frac{\partial^2[Ca^{2+}]}{\partial z^2} - Sp \cdot J_{CaCO_3} \quad (5)$$

$$\frac{\partial[Alk]}{\partial t} = D_{Ca} \cdot \frac{\partial^2[Alk]}{\partial z^2} - 2 \cdot Sp \cdot J_{CaCO_3} \quad (6)$$

$$\frac{\partial[^{13}CO_2]}{\partial t} = D_{CO_2} \cdot \frac{\partial^2[^{13}CO_2]}{\partial z^2} + \{-k'_{+1}[^{13}CO_2] + k'_{-1}[^{13}EIC] \cdot {}^{13}\chi \cdot [H^+] - k'_{+4}[^{13}CO_2][OH^-] + k'_{-4}[^{13}EIC] \cdot {}^{13}\chi\} \quad (7)$$

$$\frac{\partial[^{13}EIC]}{\partial t} = D_{EIC} \cdot \frac{\partial^2[^{13}EIC]}{\partial z^2} + \left\{k'_{+1}[^{13}CO_2] - k'_{-1}[^{13}EIC] \cdot {}^{13}\chi \cdot [H^+] + k'_{+4}[^{13}CO_2][OH^-] - k'_{-4}[^{13}EIC] \cdot {}^{13}\chi\right\} - Sp \cdot J_{CaCO_3} \cdot \frac{[^{13}EIC]}{[EIC]} \cdot \left({}^{13}\alpha_{CaCO_3\text{-}EIC}\right) \quad (8)$$

$$\frac{\partial[C^{18}OO]}{\partial t} = D_{CO_2} \cdot \frac{\partial^2[C^{18}OO]}{\partial z^2} + \{-b_{+1}[C^{18}OO] + 2/3b_{-1}[^{18}EIC] \cdot {}^{18}\chi \cdot [H^+] - b_{+4}[C^{18}OO][OH^-] + 2/3b_{-4}[^{18}EIC] \cdot {}^{18}\chi\} \quad (9)$$

$$\frac{\partial[^{18}EIC]}{\partial t} = D_{EIC} \cdot \frac{\partial^2[^{18}EIC]}{\partial z^2} + \{a_{+1}[CO_2]r_w - 1/3a_{-1}[^{18}EIC] \cdot {}^{18}\chi \cdot [H^+] + a_{+4}[CO_2][^{18}OH^-] - 1/3a_{-4}[^{18}EIC] \cdot {}^{18}\chi + b_{+1}[C^{18}OO] - 2/3b_{-1}[^{18}EIC] \cdot {}^{18}\chi \cdot [H^+] + b_{+4}[C^{18}OO][OH^-] - 2/3b_{-4}[^{18}EIC] \cdot {}^{18}\chi\} - Sp \cdot J_{CaCO_3} \cdot \frac{[^{18}EIC]}{[EIC]} \cdot \left({}^{18}\alpha_{CaCO_3\text{-}EIC}\right) \quad (10)$$

where $D_i \approx$ 1e-9 m^2/s is the diffusivity of species i, χ is the fraction of EIC that is HCO_3^-, J_{CaCO_3} is the growth rate of $CaCO_3$ (mol/m^2/s), Sp is the specific reactive surface area (m^2/kg-soln), and r_w is the $^{18}O/^{16}O$ of water. Reaction terms are set apart by braces {}. Following Chen et al. (2018), we write CO_3^{2-} and HCO_3^- together as EIC, assuming instantaneous isotopic equilibration between these two species because they equilibrate on a timescale of 10^{-7} sec (Zeebe and Wolf-Gladrow, 2001). The pH is calculated in the model at each time step from [DIC] and [Alk], assuming instantaneous pH adjustment to these quantities. The time

required to establish steady state in the thin film is short, less than 30 seconds, owing to the small length scale of the domain (Fig. S11).

Steady state profiles are displayed in Fig. 12. The only parameter we treat as adjustable is the specific reactive surface area (Sp), which dictates the efficiency of $CaCO_3$ precipitation. A large Sp implies many crystal nuclei and/or rough crystal surfaces and leads to lower steady state Ω values because a large precipitation flux prevents DIC accumulation (Fig. 12f). In the absence of any constraints on Sp, we report that $Sp \sim 200 \pm 100\ m^2$/kg-soln yields pH, growth rate, and Ω profiles that are most consistent with our estimates based on floe thickness and growth rate calculations (Fig. 12i), but note that a wide range of Sp values (10–1000) can be accommodated by the data.

The CO_2 flux from the atmosphere is governed by the concentration gradient of CO_2, which is very large near the surface since the CO_2 in the water is close to zero (Fig. 12a). The diffusive flux of CO_2 into the deeper pool water is very small because CO_2 hydroxylates faster than it can diffuse. The increase in DIC and removal of Ca^{2+} to $CaCO_3$ both lower the pH near the surface (Fig. 12k). Although the pH is lower, the degree of calcite supersaturation is highest near the surface (Fig. 12f) because the increase in DIC more than offsets the DIC speciation effects caused by lower pH.

The model accounts for isotopic distillation of reactants as they are converted to products. This is clearly seen in the $\delta^{13}C$ profile for CO_2 (Fig. 12g) where isotopically light CO_2 has been removed by hydroxylation, leaving behind a residual CO_2 pool with very low concentration that is extremely isotopically heavy. The abrupt return to the initial value at $z = -100$ is a consequence of the fixed concentration boundary condition in the model. Isotopic distillation does not occur for the $\delta^{18}O$ of CO_2 (Fig. 12d) because the KFF is set at 0‰, as discussed further below.

5.3.2. CO_2 hydroxylation KFFs

The thin-film model is used to inform our estimates of the kinetic fractionation factors (KFFs) related to $CO_{2(aq)}$ hydroxylation, which represents the instantaneous isotopic fractionation between the reactant $CO_{2(aq)}$ (for carbon KFF) or '$CO_{2(aq)} + OH^-$' (for the bulk oxygen KFF) and the product HCO_3^-. To begin, it is important to note that the CO_2 hydroxylation reaction is essentially unidirectional in the upper 60 μm of the model domain, where the ratio of forward to backward reaction rates is >1000 (Fig. 12c). This implies that the full kinetic fractionation is expressed in the EIC prior to it being converted to $CaCO_3$. There is, however, an additional kinetic fractionation attending the $CaCO_3$ precipitation reaction that depends on the degree of supersaturation through an equilibration index E_c (Devriendt et al., 2017). Since the degree of supersaturation is relatively modest for $Sp > 10\ m^2$/kg, the precipitation reaction is bi-directional and the precipitating $CaCO_3$ is isotopically heavier than CO_3^{2-}. This drives the isotopic composition of EIC to an isotopically lighter composition than that set by the kinetic limit of hydroxylation (Fig. 12e, h, and l),

The best-fit hydroxylation KFFs depend on the degree of distillation of EIC as it is converted to $CaCO_3$, which in turn depends on Sp (Fig. 12e and h). A small Sp leads to a small fraction of the CO_3^{2-} converting to $CaCO_3$. In this scenario, the dissolved CO_3^{2-} records the KFF and the $CaCO_3$ is offset to heavier values (Fig. 12l). By contrast, for $Sp > 100$, most of the CO_3^{2-} is converted to $CaCO_3$ and in this scenario, the $CaCO_3$ records the KFF while the CO_3^{2-} is offset to even lighter values (Fig. 12l). It may be significant that the one measurement of $\delta^{13}C$ of BSC pool water DIC gives a value of −31.5‰ (VPDB; Morrill et al., 2013), which is about 5‰ lighter than the lightest values recorded by the $CaCO_3$ and consistent with near complete conversion of CO_3^{2-} to $CaCO_3$. This suggests that, instead of the EIC, it is the solid $CaCO_3$ that records the CO_2 hydroxylation KFF. If indeed there is a near quantitative transfer of the EIC to $CaCO_3$, the carbon and oxygen KFFs estimated from the $\delta^{18}O$ and $\delta^{13}C$ of floe samples should be unaffected by their varying proportions of calcite versus aragonite.

Using the $\delta^{13}C$ values of floes at BSC and of local atmospheric CO_2 for the period 2013–2018 (NOAA CO_2 station Trinidad Head, USA- White et al. 2015), the carbon KFF related to CO_2 hydroxylation is estimated here to be -17.1 ± 0.8‰ relative to $CO_{2(aq)}$ at 17.4 ± 1.0 °C. Following the same reasoning as for carbon isotopes, a bulk oxygen KFF is estimated at -0.4 ± 1.5‰ relative to '$CO_{2(aq)} + OH^-$'. The oxygen KFF calculated relative to '$CO_{2(aq)} + OH^-$' relies on the accuracy of the OH^-/H_2O oxygen EFF. A value of -21.3 ± 2.2‰ relative to H_2O for the equilibrium isotopic composition of OH^- was used based on quantum-chemical calculations (Zeebe, 2020). Since the isotopic composition of H_2O can be directly measured with high accuracy, and since the OH^-/H_2O oxygen EFF is likely to be refined in the future, we also report the KFF relative to the sum of '$CO_{2(aq)} + H_2O$' ($KFF^* = -7.1 \pm 1.1$‰).

Kinetic isotope effects of similar magnitude have also been reported for a range of natural and synthetic carbonates formed in high pH solutions with gaseous CO_2 as the main DIC source. We reviewed the literature to compile a set of carbon and oxygen KFFs within a consistent framework. The revised KFF values listed in Table 7 and were calculated by taking into consideration the following:

(i) The temporal and geographical variability in the $\delta^{13}C$ and $\delta^{18}O$ of atmospheric CO_2 (Trolier et al., 1996; Keeling et al., 2001) for studies where the DIC source was atmospheric CO_2.
(ii) $CO_{2(g)}$ distillation effects were corrected for in (semi-) closed system experiments (where possible) while an infinite $CO_{2(g)}$ pool was assumed for fully open experiments.
(iii) Values for the equilibrium fractionation factors (EFFs) between $CO_{2(aq)}$ and $CO_{2(g)}$ of −1.1‰ and −0.3‰ were applied for carbon (Vogel et al., 1970) and oxygen (Beck et al., 2005; Barkan and Luz. 2012) isotopes, respectively.

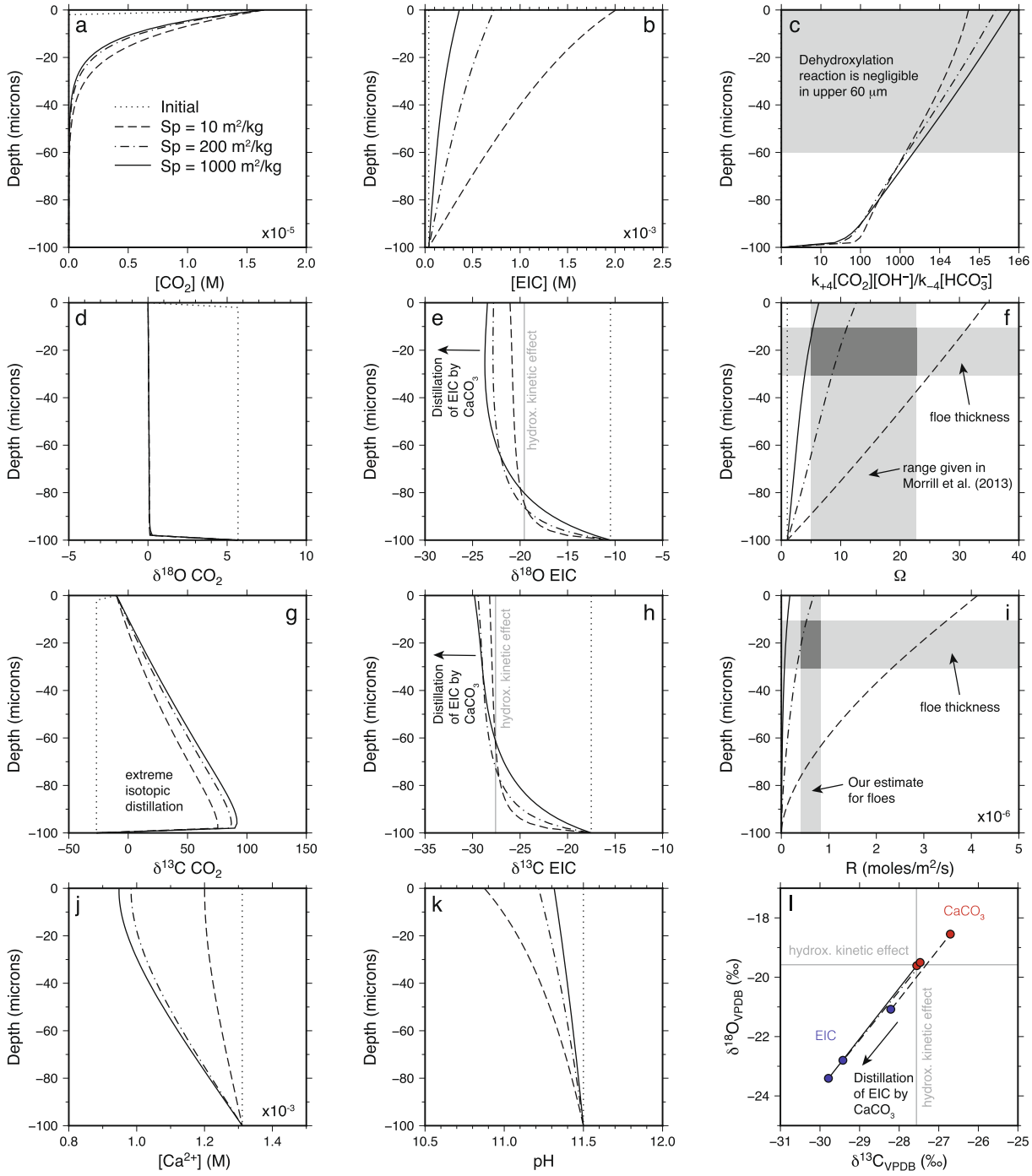

Fig. 12. Results of the thin-film model. Curves represent steady state profiles for different values of Sp. **(a)-(k)** Dissolved CO_2 is assumed to be in local chemical and isotopic equilibrium with the atmosphere at z = 0. As CO_2 diffuses downward, it reacts with OH^- to form isotopically light EIC, resulting in residual CO_2 that is isotopically heavy. The increase in DIC near the surface increases the supersaturation while decreasing the pH. Precipitation of $CaCO_3$ decreases $[Ca^{2+}]$ and EIC near the surface. **(l)** The light isotope limits of EIC and $CaCO_3$ are determined by the KFFs for hydroxylation and the proportion of CO_3^{2-} that is converted to $CaCO_3$. A large Sp implies near complete conversion with concomitant isotopic distillation of CO_3^{2-} to values lighter than given by the KFF. In this case, the $CaCO_3$ records the isotopic composition of hydroxylated HCO_3^-.

For carbon isotopes, laboratory experiments suggest a KFF between -11.8 ± 0.5‰ and -17.0 ± 0.5‰ (Table 7, Fig. 13a, Craig, 1953; Usdowski and Hoefs, 1986; Clark et al., 1992; Dietzel et al., 2009; Böttcher et al., 2018) while field data suggest a very consistent KFF of between -16.9 ± 1.3‰ and -17.2 ± 0.6‰ (Table 7, Fig. 13a; Clark et al., 1992; Mervine et al., 2014; Falk et al., 2016; this study). Only three studies suggest a significantly lower carbon

Table 7
Compilation of CO_2 hydroxylation KFF's.

Reference	Study type	Mineral	T (℃)	±	pH	$\delta^{13}C$ (‰ VPDB)				Carbon KFF*		$\delta^{18}O$ (‰ VSMOW)						Oxygen bulk KFF*			
						$CO_{2\ (g)}$	±	mineral	±	vs $CO_{2\ (aq)}$ [h]	±	H_2O	±	$CO_{2\ (g)}$	±	mineral	±	vs '$CO_{2\ (aq)} + OH^-$' [k]	±	vs '$CO_{2\ (aq)} + H_2O$'	±
Craig (1953)	Lab	Witherite	20	3	?	−9.1	0.1	−23.1	0.1	−13.7[i]	0.1	–	–	–	–	–	–	–	–	–	–
Usdowski & Hoefs (1986)	Lab	Witherite	18	1	10.0	−7.7[a]	0.3	−25.7	0.4	−17.0	0.5	–	–	–	–	–	–	–	–	–	–
Clark et al. (1992)	Lab	Witherite	22	2	>11.5	−10.5	0.4	−25.0	1.0	−13.9[i]	1.1	−6.7	0.1	36.6	0.3	6.8	1.0	−8.5	1.4	−15.0	0.2
Clark et al. (1992)	Lab	Witherite	22	2	12.8	−45.2	0.1	−61.3	0.1	−16.2[i]	0.1	−11.9	0.1	11.1	0.1	−11.2	0.1	−7.9	0.8	−14.5	0.1
Dietzel et al. (2009)	Lab	Calcite	5	1	10.5	–	–	–	–	–	–	−9.6	0.1	35.7[j]	0.1	3.4	0.1	−10.0	0.9	−16.8	0.1
Böttcher et al. (2018)	Lab	Witherite	4	1	12.4	−8.6[b]	0.5	−21.4	0.1	−11.8	0.5	−7.0	0.1	30.9[b]	1.0	8.3	0.1	−2.8	1.5	−9.8	0.7
Böttcher et al. (2018)	Lab	Witherite	21	1	12.4	−8.6[b]	0.5	−25.3	0.1	−15.8	0.5	−7.0	0.1	30.9[b]	1.0	10.0	0.1	−1.5	1.4	−8.1	0.7
Clark et al. (1992)	Field	Calcite	28	6	11.5	−7.5	1.1	−24.5[c]	0.2	−17.0	1.1	−0.5	0.1	31.1[b]	0.5	14.3[c]	0.9	0.4	1.4	−6.2	0.4
Clark et al. (1992)	Field	Calcite	28	6	11.5	−7.5	1.1	−25.3[d]	0.7	−16.9	1.3	−0.9	0.1	31.1[b]	0.5	13.5[d]	0.1	−0.3	1.0	−6.8	0.4
Mervine et al. (2014)	Field	Calcite	28	6	11.0	−8.6[b]	0.2	−26.5[e]	0.3	−17.0	0.3	−0.5	1.5	31.1[b]	0.5	14.4[e]	0.4	0.5	1.1	−6.0	0.8
Falk et al. (2016)	Field	Arag. & calcite	27	5	11.7	−8.6[b]	0.2	−26.8[f]	0.6	−17.2	0.6	0.1	1.0	31.1[b]	0.5	14.0[f]	0.4	0.0	1.1	−6.6	0.7
This study	Field	Arag. & calcite	17	1	11.0	−8.6[b]	0.4	−26.6[g]	0.7	−17.1	0.8	−5.7	1.2	30.9[b]	1.0	11.4[g]	0.4	−0.4	1.5	−7.1	1.1

[*] Note: KFFs are expressed as $\varepsilon = (\alpha\text{-}1) \times 1000$.
[a] Keeling et al. (2001), station La Jolla (CA, USA).
[b] NOAA CO_2 global network station closest to study site (incl. 2017 Ochsenkopf, Germany; 2007–2012 Ketura, Israel; 2007–2012 Kaashidhoo, Maldives; 2013–2018 Trinidad Head, USA).
[c] average modern crust 'NJ' samples.
[d] average modern crust 'clinic' samples.
[e] average of two lowest 'crust' samples.
[f] average of 'WHOI surface film' samples.
[g] average 'BSC floes' samples.
[h] $CO_{2(aq)}$–$CO_{2(g)}$ carbon fractionation of 1.1‰ from Vogel et al. (1970).
[i] corrected for distillation effect.
[j] CO_2-H_2O isotopic equilibrium assumed.
[k] calculated with OH^-−H_2O EFF values from Zeebe (2020).

KFF than −17‰ (Craig, 1953; the open system experiment of Clark et al., 1992; 4°C experiments of Böttcher et al., 2018). Lower apparent KFF in laboratory studies may be caused by a distillation of the CO_2 source or thermal differences bewteen compressed air from the laboratory and the solution. Alternatively, the carbon KFF may be negatively correlated with temperature (Fig. 13a, $r^2 = 0.53$, p-value = 0.01), though this hypothesis is not supported by theoretical work (Guo, 2019). Based on field studies alone, where atmospheric CO_2 distillation is unlikely to occur, our best estimate for the carbon KFF related to the CO_2 hydroxylation reaction is −17.0 ± 0.3‰ (2σ; $n = 5$) over the 17–28 °C temperature range.

For oxygen isotopes, most studies suggest a bulk KFF close to zero or slightly negative expressed relative to the sum of reactants '$CO_{2(aq)} + OH^-$' (−2.8 ± 1.5‰ to +0.5 ± 1.1‰, Clark et al., 1992; Mervine et al., 2014; Falk et al., 2016; Böttcher et al., 2018; this study). However, the experimental work of Clark et al. (1992) and Dietzel et al. (2009) suggests a negative bulk oxygen KFF of between −10.0 ± 0.9‰ and −7.9 ± 0.8‰ (not shown in Fig. 13b and 13c). Although the cause of this discrepancy is unclear, the excellent agreement in the bulk oxygen KFF value among all the field studies suggests an oxygen KFF of 0.0 ± 0.8‰ over the 17–28 °C temperature range (Fig. 13b). This result is consistent with theoretical calculations for a bulk KFF close to 0‰ (Sade and Halevy, 2017, 2018; Guo, 2019).

Oxygen KFF values were also calculated relative to '$CO_2 + H_2O$' (KFF*, Fig. 13c) to avoid the uncertainty related to the calculated $^{18}O/^{16}O$ ratio of OH^-. The KFF* from field studies average −6.6 ± 0.9‰ over the 17–28 °C temperature range. The lower KFF* calculated from the experimental result at 5 °C (Böttcher et al., 2018) may indicate a positive temperature effect on the KFF* of ~0.14‰/°C but this result will need confirmation with additional data. Such a temperature dependence would be in part caused by the effect of temperature on the OH^-/H_2O oxygen EFF (i.e. ~+0.06‰/°C; Zeebe, 2020).

5.3.3. Box model for the pools

The thin-film model is useful for quantifying the hydroxylation KFFs and understanding the isotopically light end of the array. To understand the overall trend we consider the different sources of DIC and forms of carbonate precipitating in the pools as a whole. Unlike the thin film at the surface, it takes much longer than 30 seconds to establish steady state in the larger volume (10–1000 L) pools. For this part of the system we apply a box model with four fluxes representing the sources and sinks of DIC: (1) an atmospheric flux, (2) a replenishment flux from the spring, (3) a flux from the adjacent low-pH (8.7) creek, and (4) a calcium carbonate precipitation flux. For the atmospheric flux of DIC to the pool (J_{atm}) we use a value of 6×10^{-7} mol/m^2/s based on the steady state EIC gradient in the thin-film model and the measured growth rates of the floes. For the replenishment flux (F_{spr}), we use the inferred pool resupply rate of ~1 ml/s (see Section 5.1). For the $CaCO_3$ precipitation flux and the $CaCO_3$-CO_3 fractionation factors, we use the same formulation as in the thin-film model.

There are eight differential equations in the box model:

$$\frac{\partial[CO_2]}{\partial t} = \{\text{reaction terms, Eq. (3)}\} + \frac{F_{spr}}{V_{pool}} \times ([CO_2]_{spr} - [CO_2]) + \frac{F_{cr}}{V_{pool}}([CO_2]_{cr} - [CO_2]) \quad (11)$$

$$\frac{\partial[EIC]}{\partial t} = \{\text{reaction terms, Eq. (4)}\} + \frac{J_{atm} \cdot SA_{pool}}{V_{pool}} + \frac{F_{spr}}{V_{pool}}([EIC]_{spr} - [EIC]) + \frac{F_{cr}}{V_{pool}}([EIC]_{cr} - [EIC]) - J_{CaCO_3} \cdot Sp \quad (12)$$

$$\frac{\partial[Ca^{2+}]}{\partial t} = \frac{F_{spr}}{V_{pool}}([Ca^{2+}]_{spr} - [Ca^{2+}]) + \frac{F_{cr}}{V_{pool}} \times ([Ca^{2+}]_{cr} - [Ca^{2+}]) - J_{CaCO_3} \cdot Sp \quad (13)$$

$$\frac{\partial[Alk]}{\partial t} = \frac{F_{spr}}{V_{pool}}([Alk]_{spr} - [Alk]) + \frac{F_{cr}}{V_{pool}}([Alk]_{cr} - [Alk]) - 2 \cdot J_{CaCO_3} \cdot Sp \quad (14)$$

$$\frac{\partial[^{13}CO_2]}{\partial t} = \{\text{reaction terms, Eq.7}\} + \frac{F_{spr}}{V_{pool}} \times ({}^{13}R_{CO_{2(spr)}}[CO_2]_{spr} - [^{13}CO_2]) + \frac{F_{cr}}{V_{pool}} \times ({}^{13}R_{CO_{2(cr)}}[CO_2]_{cr} - [^{13}CO_2]) \quad (15)$$

$$\frac{\partial[^{13}EIC]}{\partial t} = \{\text{reaction terms, Eq. (8)}\} + \frac{J_{atm} \cdot SA_{pool}}{V_{pool}} \cdot ({}^{13}R_{EIC_{(hydrox)}}) + \frac{F_{spr}}{V_{pool}}\left({}^{13}R_{EIC_{(spr)}}[EIC]_{spr} - [^{13}EIC]\right) + \frac{F_{cr}}{V_{pool}}\left({}^{13}R_{EIC_{(cr)}}[EIC]_{cr} - [^{13}EIC]\right) - J_{CaCO_3} \cdot Sp \cdot \frac{[^{13}EIC]}{[EIC]} \cdot ({}^{13}\alpha_{CaCO_3\text{-}EIC}) \quad (16)$$

$$\frac{\partial[C^{18}OO]}{\partial t} = \{\text{reaction terms, Eq. (9)}\} + \frac{F_{spr}}{V_{pool}} \times ({}^{18}R_{CO_{2(spr)}}[CO_2]_{spr} - [C^{18}OO]) + \frac{F_{cr}}{V_{pool}} \times ({}^{18}R_{CO_{2(cr)}}[CO_2]_{cr} - [C^{18}OO]) \quad (17)$$

$$\frac{\partial[^{18}EIC]}{\partial t} = \{\text{reaction terms, Eq. (10)}\} + \frac{J_{atm} \cdot SA_{pool}}{V_{pool}} \cdot ({}^{18}R_{EIC_{(hydrox)}}) + \frac{F_{spr}}{V_{pool}} \times ({}^{18}R_{EIC_{(spr)}}[EIC]_{spr} - [^{18}EIC]) + \frac{F_{cr}}{V_{pool}} \times ({}^{18}R_{EIC_{(cr)}}[EIC]_{cr} - [^{18}EIC]) - J_{CaCO_3} \cdot Sp \cdot \frac{[^{18}EIC]}{[EIC]} \cdot ({}^{18}\alpha_{CaCO_3\text{-}EIC}) \quad (18)$$

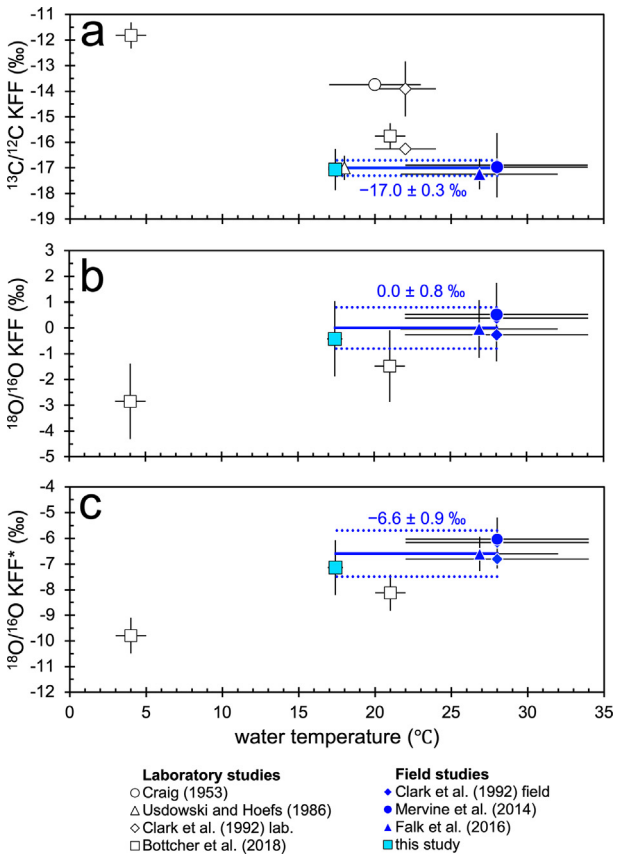

Fig. 13. Compilation of kinetic isotope fractionation factors (KFF) related to the CO_2 hydroxylation reaction determined from laboratory and field studies. **(A)** Carbon KFF estimates showing a consistent cluster of field data at around ~ −17.0 ± 0.3‰ and more scattered KFF estimates from laboratory studies. **(B)** Oxygen KFF estimates expressed relative to the weighted sum of reactants 'CO_2 + OH^-' showing consistent field data at 0.0 ± 0.8‰ but lower estimates from the laboratory study of Böttcher et al. (2018). (C) Oxygen KFF* estimates expressed relative to the weighted sum of 'CO_2 + H_2O' with field data averaging −6.6 ± 0.9‰.

As a reference case, we use $SA_{pool} = 1\ m^2$, $Sp = 0.1\ m^2/L$ and $V_{pool} = 100L$. This value of Sp is much smaller than the value used in the thin-film model because $V_{pool} \gg V_{film}$ and there is a much higher surface area density of $CaCO_3$ in the thin film than in the bulk pool. The atmospheric DIC flux is $F^*_{atm} = 6 \times 10^{-7}$ mol/s, which is much greater than the spring DIC replenishment flux of $F^*_{spring} = F_{spring}[DIC]_{spring} = 3.5 \times 10^{-8}$ mol/s, implying that the isotopic results are not sensitive to the $\delta^{13}C$ of spring water because of its low DIC concentration. The spring flux still plays an important role, however, because it resupplies dissolved Ca^{2+} at a rate of 1.5×10^{-6} mol/s, which is comparable to the DIC flux from the atmosphere.

The results of running the model to steady state for different values of F^*_{creek} at constant F^*_{atm} and F^*_{spring} are displayed in Fig. 14. In each panel there are three curves corresponding to different initial pH values of the pool (Fig. 14a). The change in steady state pH, Ca^{2+}, and [DIC] occurs approximately where F^*_{creek} overtakes F^*_{atm} (Fig. 14a–c). The steady state Ω and surface area normalized growth rate can be tuned by adjusting SA_{pool}, Sp, and V_{pool} (Supplement), but since these parameters have a limited effect on the overall isotopic results, they will not be discussed further.

The isotopic results of the box model are displayed in Fig. 14f and Fig. 15. The light endmember of the array corresponds to low F^*_{creek}/F^*_{atm}. As the creek DIC flux increases, the pH decreases (shown by red circled numbers for the $pH_i = 12.0$ case in Fig. 15) and the $\delta^{18}O$-$\delta^{13}C$ values move away from the kinetic limit and up the 1:1 line. Importantly, the pH remains above 11 for the entire part of the array below the equilibrium calcite line. The extreme heavy end of the array corresponds to high F^*_{creek}/F^*_{atm} and steady state pH values below ~11. An outcome of mixing of creek DIC to the high pH pool is that the oxygen isotopic composition of HCO_3^- can become isotopically distilled to higher-than-equilibrium values as it is converted to the isotopically lighter CO_3^{2-}. This can account for the cluster of carbonate samples exhibiting higher-than-equilibrium values. The extent of distillation is particularly sensitive to the initial pH, or more generally, the relative alkalinities of the spring versus creek water.

In Fig. 15, the CO_2 distillation trajectory illustrates what would occur if all incoming atmospheric CO_2 were to undergo hydroxylation without an opportunity for atmospheric equilibrium exchange. The isotopic data show no evidence to support this, indicating that CO_2 exchanges with the atmosphere faster than it is hydroxylated into HCO_3^-. This result supports the local equilibrium assumption in the thin-film model and our treatment in the box model of CO_2 entering the bulk pool as EIC with an isotopic composition reflecting the kinetic limit of CO_2 hydroxylation. The DIC equilibration trajectory shows the isotopic behavior of the EIC as the ratio between HCO_3^- dehydroxylation and CO_2 hydroxylation increases from 0 to 1. The isotopic data show no evidence of partial equilibration, indicating that the HCO_3^- dehydroxylation rate is negligible relative to the CO_2 hydroxylation rate. This is supported by modeling results, which indicate that an unrealistic $V_{pool}/SA_{pool} > 1000$ is required in the model framework to yield an appreciable equilibration trajectory (Fig. S12).

5.4. Comparison to Oman carbonates

A quantitative understanding of the calcium carbonate $\delta^{13}C$-$\delta^{18}O$ array at the Cedars enables us to explain the similarities and differences in isotopic data between carbonates from the Cedars (Fig. 8) and from Oman (Fig. 1). The $\delta^{18}O/\delta^{13}C$ slopes from these two arrays are indistinguishable and follow a 1:1 line but there are noteworthy differences. The highest $\delta^{18}O$ and $\delta^{13}C$ values in the Oman array are about 5‰ and 8‰ greater than at The Cedars, respectively. The higher heavy end-member of Oman carbonates can be explained by higher and more variable atmospheric/surface water $\delta^{18}O$ and DIC $\delta^{13}C$ (large area of 50 x 200 km, Falk et al., 2016). In contrast, there are only minor differences in the light isotope limits between the Cedars (min $\delta^{13}C$ ~ −27‰, min $\delta^{18}O$ ~ −20‰) and Oman

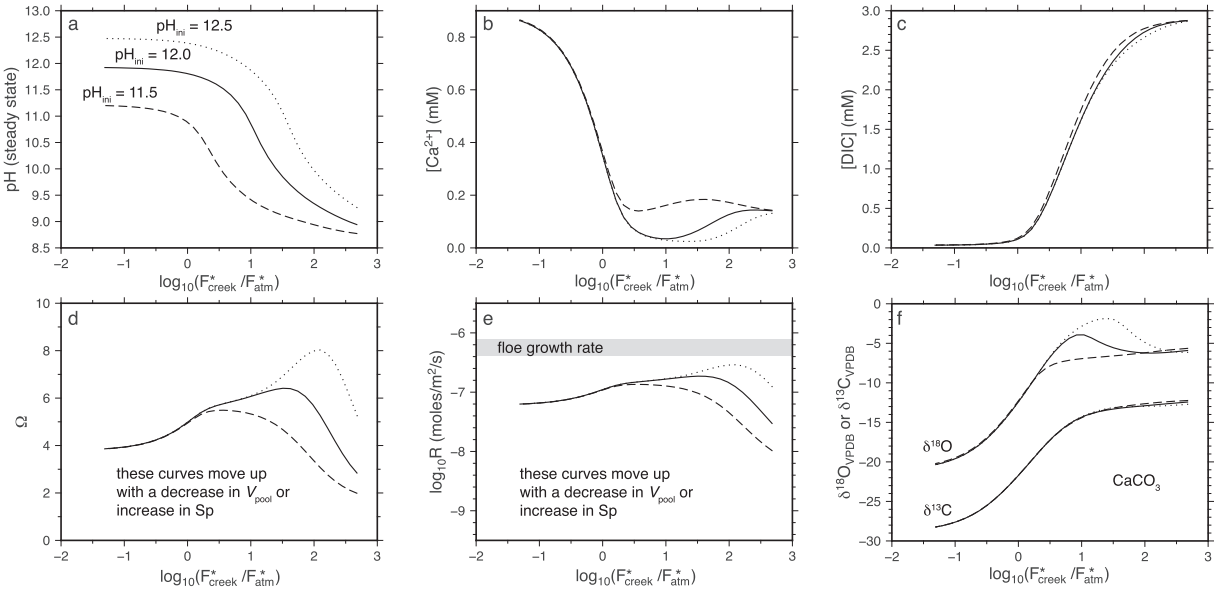

Fig. 14. Box model results for pools of high pH water at The Cedars. **(a)-(f)** Steady state composition of the pool as a function of F^*_{creek} at fixed F^*_{spring} and F^*_{atm}.

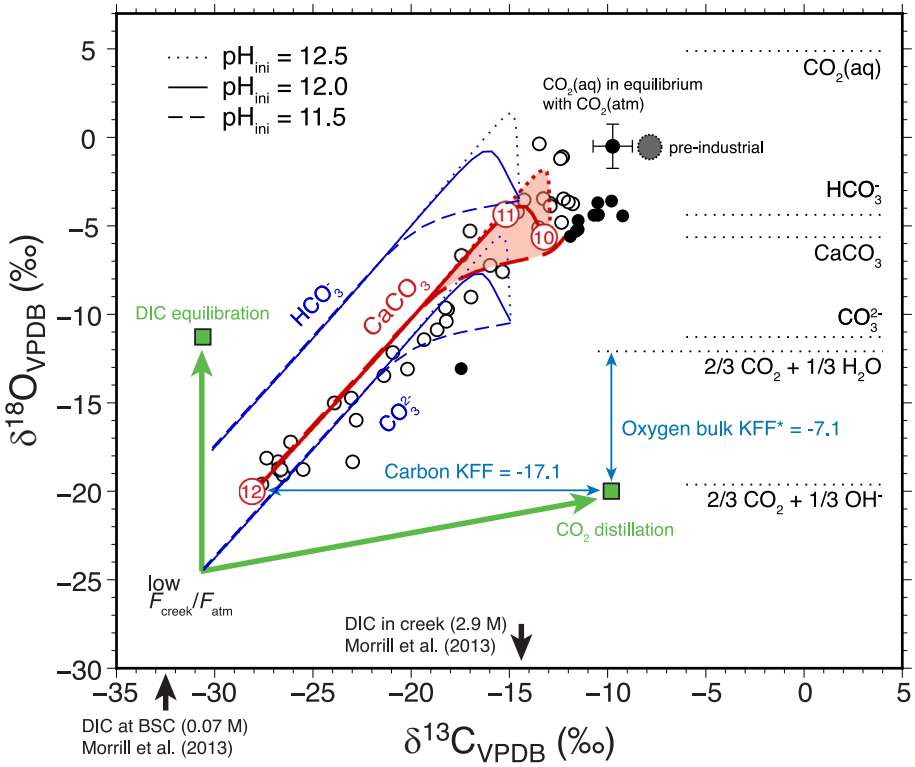

Fig. 15. Box model results for pools of high pH water at The Cedars using the same parameters as in Fig. 14. The circles with red numbers represent the pH values along the $pH_{ini} = 12$ curve and show that pH remains high along the full array. Higher-than-equilibrium calcite forms when HCO_3^- from the creek is isotopically distilled during conversion to CO_3^{2-}, which is then inherited by the $CaCO_3$. The green arrows show the trajectories of DIC equilibration and CO_2 distillation (all incoming CO_2 converted to HCO_3^-) for comparison.

(min $\delta^{13}C \sim -27‰$, min $\delta^{18}O \sim -18‰$). The almost identical $\delta^{13}C$ light end-members of these geographically distant sites is not coincidental and reflects the relatively homogenous $\delta^{13}C$ of atmospheric CO_2 worldwide (currently $-8.6 \pm 0.5‰$, NOAA CO_2 global network) and the likely limited temperature sensitivity of the carbon KFF related to CO_2 hydroxylation (Section 5.3.2). Modern carbonates forming in alkaline springs at the atmosphere-water interface therefore record the carbon isotopic composition of atmospheric CO_2. For the $\delta^{18}O$ light end-member, differences between sites are also expected to be small since the $\delta^{18}O$ of atmospheric CO_2 is also very similar in temperate and tropical regions (Trolier et al., 1996). However, calcium carbonates formed from hydroxylated CO_2 obtain one oxygen atom from OH^-, making their $\delta^{18}O$ value moderately sensitive to the solution $\delta^{18}O$. A ~ 5‰ difference in water $\delta^{18}O$ between the Cedars and Oman springs (based on the heavy $\delta^{18}O$ end-members) would result in a difference of ~ 1.7‰ for the light $\delta^{18}O$ end-members, in good agreement with the observed ~ 2‰ difference between sites. Additional differences in the light end-members for oxygen isotopes may be caused by a temperature effect on the CO_2 hydroxylation KFF but this is not yet resolved.

5.5. Potential paleoenvironmental applications

The samples from old (unknown age) laminated calcium carbonate from BSC are shifted to the right of the array of modern carbonates (Fig. 8 and Fig. 15). A likely explanation is that these carbonates formed at a time when atmospheric CO_2 had a heavier, pre-industrial $\delta^{13}C$ value, as depicted in Fig. 8. This feature of the data suggests that the $\delta^{13}C$ of pre-industrial atmospheric CO_2 may be recoverable from ancient travertine, some of which is as old as 7000 years at The Cedars (^{14}C ages 950–7100 years, Table S4).

The $\delta^{18}O$ values of old travertines and most modern travertines are close to the end-member $\delta^{18}O$ value reflecting HCO_3^- isotopically equilibrated with creek water (based EFF values from Beck et al., 2005). This suggests surface water DIC is the dominant carbon supply to travertine formation at The Cedars (rather than atmospheric CO_2). Hence, old travertines $\delta^{18}O$ at The Cedars are expected to primarily reflect the oxygen isotope composition of past precipitation and surface/creek water temperature.

6. CONCLUSIONS

We investigated the textural and isotopic characteristics of carbonates that precipitate from ultrabasic (pH ~ 11–12) spring pools at The Cedars, California. The pools are fed by spring waters that have low [DIC], low Mg/Ca, and relatively high [Ca^{2+}] as a consequence of serpentinization and Mg-carbonate precipitation in the subsurface. Once the spring water reaches the surface, CO_2 from the atmosphere enters and a thin film of $CaCO_3$ crystallizes and is held in place by surface tension. The initial polymorph to crystallize is aragonite, followed by calcite on the underside of the floe as it thickens. The preference of aragonite over calcite in this case is likely controlled by pH and not by high Mg/Ca ratio or high supersaturation.

Calcium isotopic fractionation between $CaCO_3$ and the host solution is sensitive to growth rate. The $\Delta^{44/40}Ca$ values retrieved from five carbonate-water pairs are indistinguishable, with an average value of $-0.75 \pm 0.07‰$ (±95% confid.). The $CaCO_3$ growth rates are based on thickness measurements of surface floes of known age and are estimated to be the range of 4.8×10^{-7} mol/m^2/sec to 8.0×10^{-7} mol/m^2/sec. This value is in good agreement with the growth rate dependence of $\Delta^{44/40}Ca$ determined from laboratory experiments (Tang et al., 2008; Watkins et al., 2017) and modeling (DePaolo, 2011; Nielsen et al., 2012).

Calcium carbonates display an extreme range (>20‰) in carbon and oxygen isotope compositions. The $\delta^{13}C$ and $\delta^{18}O$ values co-vary along a 1:1 line which trends toward the isotopic composition of isotopically equilibrated DIC from surface waters and pointing toward atmospheric CO_2. Most of the samples are lower in $\delta^{18}O$, some by as much as 15‰, than the expected equilibrium value at 17.4 °C. The extreme light isotope enrichments are an expression of the isotopically light OH^- ions combining with incoming of CO_2 to form HCO_3^-. The HCO_3^- rapidly deprotonates and is nearly quantitatively converted to CO_3^{2-} ions, which then react with Ca^{2+} to precipitate $CaCO_3$. We estimate the hydroxylation KFF's to be about −17‰ relative to $CO_{2(aq)}$ for carbon isotopes and −7‰ relative to '$CO_{2(aq)} + H_2O$' for oxygen isotopes. These compare favorably to other estimates based on analysis of natural samples, but discrepancies remain between field and laboratory studies.

We adapted the kinetic isotopic fractionation model from Chen et al. (2018) to further investigate mechanisms of carbonate precipitation and kinetic isotope fractionation. The DIC in solution evolves chemically and isotopically according to the reaction rate equations in the $CaCO_3$-DIC-H_2O system. Using known (or reasonably well constrained) isotope-specific reaction rate constants, along with values for the fluxes that are constrained from the literature and our own measurements, the model reproduces the 1:1 co-variation if (1) the residence time of DIC in solution is much shorter than the equilibration time; (2) CO_2 exchange with the atmosphere is efficient so that the incoming CO_2 does not become isotopically distilled when being converted to HCO_3^-; and (3) the isotopic composition of the isotopically equilibrated spring and creek waters also lies near the 1:1 line defined by the composition of atmospheric CO_2 and the isotopically lightest data points. The model can also match the observation that some of the carbonates are isotopically heavier than the equilibrium value, owing to isotopic distillation of HCO_3^- from creek water as it is nearly quantitatively converted to CO_3^{2-} during mixing with pool water.

Declaration of Competing Interest

The authors declare that they have no known competing financial interests or personal relationships that could have appeared to influence the work reported in this paper.

ACKNOWLEDGEMENTS

We are grateful to Roger Raiche for access and transport to The Cedars and for guiding us to the various fascinating spring features at The Cedars. We thank Shaun T. Brown for his occasional assistance in the field, and for his advice on Ca isotopic measurement. We gratefully thank Peter Kelemen (Columbia Univ.) for providing the ^{14}C ages of travertine samples reported in the Supplement. JMW was supported by the National Science Foundation under grant no. EAR1749183. This research was supported by the US Department of Energy, Office of Science, Office of Basic Energy Sciences under Award No. DE-AC02-05CH11231 to Lawrence Berkeley National Laboratory.

APPENDIX A. SUPPLEMENTARY MATERIAL

Supplementary data and information to this article can be found online at https://doi.org/10.1016/j.gca.2021.01.003.

REFERENCES

Adkins J. F., Boyle E. A., Curry W. B. and Lutringer A. (2003) Stable isotopes in deep-sea corals and a new mechanism for "vital effects". *Geochim. Cosmochim. Acta* **67**, 1129–1143.

Barkan E. and Luz B. (2012) High-precision measurements of $^{17}O/^{16}O$ and $^{18}O/^{16}O$ ratios in CO_2. *Rapid Commun. Mass Spectrom.* **26**, 2733–2738.

Barnes I., LaMarche V. C. and Himmelberg G. (1967) Geochemical evidence of present-day serpentinization. *Science* **156**, 830–832.

Barnes I. and O'Neil J. (1969) The Relationship between Fluids in Some Fresh Alpine-Type Ultramafics and Possible Modern Serpentinization, Western United States. *Geol. Soc. of Amer. Bull.* **80**, 1947–1960.

Barnes I., O'Neil J. and Trescases J. J. (1978) Present day serpentinization in New-Caledonia, Oman and Yugoslavia. *Goechim. Cosmochim. Acta* **42**, 144–145.

Beck W. C., Grossman E. L. and Morse J. W. (2005) Experimental studies of oxygen isotope fractionation in the carbonic acid system at 15, 25, and 40C. *Geochim. Cosmochim. Acta* **69**, 3493–3503.

Blake, M. C., Jr., Graymer, R. W. and Stamski, R. E. (2002) Geologic map and map database of western Sonoma, northernmost Marin, and southernmost Mendocino Counties, California: U.S. Geological Survey Miscellaneous Field Studies Map MF-2402, version 1.0, scale 1:62,500.

Blake, M. C., Jr., Bailey, E. H. and Wentworth, C. M. (2012) The Cedars ultramafic mass, Sonoma County, California. U.S. Geological Survey Open-File Report, 2012-1164, 13p.

Böttcher M. E., Neubert N., Escher P., von Allmen K., Samankassou E. and Nägler T. F. (2018) Multi-isotope (Ba, C, O) partitioning during experimental carbonatization of a hyper-alkaline solution. *Chemie der Erde* **78**, 241–247.

Bottinga Y. (1968) Calculation of fractionation factors for carbon and oxygen isotopic exchange in the system calcite-carbon dioxide-water. *J. Phys. Chem.* **72**, 800–808.

Chen S., Gagnon A. C. and Adkins J. F. (2018) Carbonic anhydrase, coral calcification and a new model of stable isotope vital effects. *Geochim. Cosmochim. Acta* **236**, 179–197.

Choi S. H., Shervais J. W. and Mukasa S. B. (2008) Supra-subduction and abyssal mantle peridotites of the Coast Range ophiolite, California. *Contrib. Mineral. Petrol.* **156**, 551–576.

Clark I. D. and Fontes J.-C. (1990) Palaeoclimatic reconstruction in northern Oman based on carbonates from hyperalkaline groundwaters. *Quat. Res.* **33**, 320–336.

Clark I. D. and Lauriol B. (1992) Kinetic enrichment of stable isotopes in cryogenic calcites. *Geochim. Cosmochim. Acta* **102**, 217–228.

Clark I. D., Fontes J.-C. and Fritz P. (1992) Stable isotope disequilibria in travertine from high pH waters: Laboratory investigations and field observations from Oman. *Contrib. Mineral. Petrol.* **56**, 2041–2050.

Coleman R. G. (2000) Prospecting for ophiolites along the California continental margin. In *Ophiolites and Oceanic Crust: New Insights from Field Studies and the Ocean Drilling Program. Geological Society of American Special Paper*, vol. 349 (eds. Y. M. Dilek, E. M. Moores, D. Elthon and A. Nicolas), pp. 351–364.

Coplen T. B. (2007) Calibration of the calcite-water oxygen-isotope geothermometer at Devils Hole, Nevada, a natural laboratory. *Geochim. Cosmochim. Acta* **71**, 3948–3957.

Craig H. (1953) The geochemistry of the stable carbon isotopes. *Geochim. Cosmochim. Acta* **3**, 53–92.

Daëron M., Guo W., Eiler J., Genty D., Blamart D., Boch R., Drysdale R., Maire R., Wainer K. and Zanchetta G. (2011) ^{13}C-^{18}O clumping in speleothems: Observations from natural caves and precipitation experiments. *Geochim. Cosmochim. Acta* **75**, 3303–3317.

Daëron M., Drysdale R. N., Peral M., Huyghe D., Blamart D., Coplen T. B., Lartaud F. and Zanchetta G. (2019) Most Earth-surface calcites precipitate out of isotopic equilibrium. *Nature Comm.* **10**.

DePaolo D. J. (2011) Surface kinetic model for isotopic and trace element fractionation during precipitation of calcite from aqueous solutions. *Geochim. Cosmochim. Acta* **75**, 1039–1056.

Devriendt L. S., Watkins J. M. and McGregor H. V. (2017) Oxygen isotope fractionation in the $CaCO_3$-DIC-H_2O system. *Geochim. Cosmochim. Acta* **214**, 115–142.

Dietzel M., Tang J., Leis A. and Köhler S. J. (2009) Oxygen isotopic fractionation during inorganic calcite precipitation – effects of temperature, precipitation rate and pH. *Chem. Geol.* **268**, 107–115.

DOE (1994) Handbook of methods for the analysis of the various parameters of the carbon dioxide system in seawater; version 2. ORNL/CDIAC.

Falk E. S., Guo W., Paukert A. N., Matter J. M., Mervine E. M. and Kelemen P. B. (2016) Controls on the stable isotope compositions of travertine from hyperalkaline springs in Oman: Insights from clumped isotope measurements. *Geochim. Cosmochim. Acta* **192**, 1–28.

Guo W. (2019) Kinetic clumped isotope fractionation in the DIC-H_2O-CO_2 system: patterns, controls and implication. *Geochim. Cosmochim. Acta* **268**, 230–257.

Harms, P. A. (2015) Distribution of Tritium in Precipitation and Surface Water in California. MS Thesis, Calif. State Univ. East Bay.

Hermoso M., Horner T. J., Minoletti F. and Rickaby R. E. M. (2014) Constraints on the vital effect in coccolithophore and dinoflagellate calcite by oxygen isotopic modification of seawater. *Geochim. Cosmochim. Acta* **141**, 612–627.

Huang S., Farkas J. and Jacobsen S. B. (2010) Calcium isotopic fractionation between clinopyroxene and orthopyroxene from mantle peridotites. *Earth Planet. Sci. Lttrs.* **292**, 337–344.

Jones B. (2017) Review of calcium carbonate polymorph precipitation in spring systems. *Sed. Geol.* **353**, 64–75.

Kawano J., Shimobayashi N., Miyake A. and Kitamura M. (2009) Precipitation diagram of calcium carbonate polymorphs: its construction and significance. *J. Phys.: Condens. Matter* **21**.

Keeling, C. D., Piper, S. C., Bacastow, R. B., Wahlen, M., Whorf, T. P., Heimann, M. and Meijer, H. A. (2001) Exchanges of atmospheric CO_2 and $^{13}CO_2$ with the terrestrial biosphere and oceans from 1978 to 2000. I. Global aspects, SIO Reference Series, No. 01-06, Scripps Institution of Oceanography, San Diego, pp. 88.

Kelemen P. B., Matter J., Streit E. E., Rudge J. F., Curry W. B. and Blusztajn J. (2011) Rates and mechanisms of mineral carbonation in peridotite: natural processes and recipes for enhanced, in situ CO_2 capture and storage. *Ann. Rev. Earth Plane. Sci.* **39**, 545–576.

Kim S.-T., Hillaire-Marcel C. and Mucci A. (2006) Mechanisms of equilibrium and kinetic oxygen isotope effects in synthetic aragonite at 25 ℃. *Geochim. Cosmochim. Acta* **70**, 5790–5801.

Kim S.-T., O'Neil J. R., Hillaire-Marcel C. and Mucci A. (2007) Oxygen isotope fractionation between synthetic aragonite and water: influence of temperature and Mg^{2+} concentration. *Geochim. Cosmochim. Acta* **71**, 4704–4715.

Kimball J. B., Dunbar R. B. and Guilderson T. P. (2014) Oxygen and carbon isotope fractionation in calcitic deep-sea corals: Implications for paleotemperature reconstructions. *Chem. Geol.* **381**, 223–233.

Leleu T., Chavagnac V., Delacour A., Noiriel C., Ceuleneer G., Aretz M., Rommevaux C. and Ventalon S. (2016) Travertine associated with hyperalkaline springs: evaluation as a proxy for paleoenvironmental conditions and sequestration of atmospheric CO_2. *J. Sed. Res.* **86**, 1328–1343.

Lian B., Hu Q., Chen J., Ji J. and Teng H. H. (2006) Carbonate biomineralization induced by soil bacterium Bacillus megaterium. *Geochim. Cosmochim. Acta* **70**, 5522–5535.

Matsumoto M., Fukunaga T. and Onoe K. (2010) Polymorph control of calcium carbonate by reactive crystallization using a microbubble technique. *Chem. Eng. Res. Design* **88**, 1624–1630.

McConnaughey T. (1989) ^{13}C and ^{18}O isotopic disequilibrium in biological carbonates: I. Patterns. *Geochim. Cosmochim. Acta* **53**, 151–162.

Meister P., Johnson O., Coresetti F. and Nealson K. H. (2011) Magnesium inhibition controls spherical carbonate precipitation in ultrabasic springwater (Cedars, California) and culture experiments. *Adv. Stromatol. Goebiol. Lect. Notes Earth Sci.* **131**.

Mervine E. M., Humphris S. E., Sims K. W., Kelemen P. B. and Jenkins W. J. (2014) Carbonation rates of peridotite in the Samail Ophiolite, Sultanate of Oman, constrained through ^{14}C dating and stable isotopes. *Geochim. Cosmochim. Acta* **126**, 371–397.

Millero F., Huang F., Graham T. and Pierrot D. (2007) The dissociation of carbonic acid in NaCl solutions as a function of concentration and temperature. *Geochim. Cosmochim. Acta* **71**, 46–55.

Mook W. (1986) ^{13}C in atmospheric CO_2. *Netherlands J. Sea Res.* **20**, 211–223.

Morrill P. L., Kuenen J. G., Johnson O. J., Suzuki S., Rietze A., Sessions A. L., Fogel M. L. and Nealson K. H. (2013) Geochemistry and geobiology of a pesent-day serpentinization site in California: The Cedars. *Goechim. Cosmochim. Acta* **109**, 222–240.

Nielsen L. C., Druhan J. L., Yang W., Brown S. T. and DePaolo D. J. (2011) Calcium Isotopes as Tracers of Biogeochemical Processes. In *Handbook of Environmental Isotope Geochemistry* (ed. M. Baskaran). Springer Berlin Heidelberg, Berlin, Heidelberg, pp. 105–124.

Nielsen L. C., DePaolo D. J. and De Yoreo J. J. (2012) Self-consistent ion-by-ion growth model for kinetic isotopic fractionation during calcite precipitation. *Geochim. Cosmochim. Acta* **86**, 166–181.

Nielsen L. C., De Yoreo J. J. and DePaolo D. J. (2013) General model for calcite growth kinetics in the presence of impurity ions. *Geochim. Cosmochim. Acta* **115**, 200–114.

O'Neil J. R. and Barnes I. (1971) C13 and O18 compositions in some fresh-water carbonates associated with ultramafic rocks and serpentinites: western United States. *Geochim. Cosmochim. Acta* **35**, 687–697.

Pinsent B. R. W., Pearson L. and Roughton F. J. W. (1956) The kinetics of combination of carbon dioxide with hydroxide ions. *Trans. Faraday Soc.* **52**(11), 1512–1520.

Romanek C. S., Grossman E. L. and Morse J. W. (1992) Carbon isotopic fractionation in synthetic aragonite and calcite: effects of temperature and precipitation rate. *Geochim. Cosmochim. Acta* **56**(1), 419–430.

Romanek C. S., Morse J. W. and Grossman E. L. (2011) Aragonite kinetics in dilute solutions. *Aquat. Geochem.* **17**, 339–356.

Sade Z. and Halevy I. (2017) New constraints on kinetic isotope effects during CO_2(aq) hydration and hydroxylation: Revisiting theoretical and experimental data. *Geochim. Cosmochim. Acta* **214**, 246–265.

Sade Z. and Halevy I. (2018) Corrigendum to "New constraints on kinetic isotope effects during CO_2(aq) hydration and hydroxylation: Revisiting theoretical and experimental data" [Geochim. Cosmochim. Acta 214 (2017) 246–265]. *Geochim. Cosmochim. Acta* **225**, 237–240.

Spero H. J., Bijma J., Lea D. W. and Bemis B. E. (1997) Effect of seawater carbonate concentration on foraminiferal carbon and oxygen isotopes. *Nature* **390**, 497–500.

Sun W., Jayaraman S., Chen W., Persson K. A. and Ceder G. (2015) Nucleation of metastable aragonite $CaCO_3$ in seawater. *Proc.s Natl. Acad. Sci.* **112**, 3199–3204.

Suzuki S., Ishii S., Wu A., Cheung A., Tenney A., Wanger G., Gijs J., Kuenen J. G. and Nealson K. H. (2013) Microbial diversity in The Cedars, an ultrabasic, ultrareducing, and low salinity serpentinizing ecosystem. *Proc.s Natl. Acad. Sci.* **110**(30), 15336–15341.

Suzuki S., Ishii S., Hoshino T., Rietze A., Tenney A., Morrill P. L., Inagaki F., Kuenen J. G. and Nealson K. H. (2017) Unusual metabolic diversity of hyperalkaliphilic microbial communities associated with subterranean serpentinization at The Cedars. *ISME J.* **11**, 2584–2598.

Tai C. Y. and Chen F. B. (1998) Polymorphism of $CaCO_3$ precipitated in a constant-composition environment. *AIChE J.* **44**, 1790–1798.

Talbot M. R. (1990) A review of the palaeohydrological interpretation of carbon and oxygen isotopic ratios in primary lacustrine carbonates. *Chem. Geol.* **80**, 261–279.

Tang J., Dietzel M., Böhm F., Kohler S. and Eisenhauer A. (2008) Sr^{2+}/Ca^{2+} and $^{44}Ca/^{40}Ca$ fractionation during inorganic calcite formation: II. Ca isotopes. *Geochim. Cosmochim. Acta* **72**, 3733–3745.

Tourney J. and Ngwenya B. T. (2009) Bacterial extracellular polymeric substances (EPS) mediate $CaCO_3$ morphology and polymorphism. *Chem. Geol.* **202**, 138–146.

Tremaine D. M., Froelich P. N. and Wang Y. (2011) Speleothem calcite farmed *in situ*: Modern calibration of $\delta^{18}O$ and $\delta^{13}C$ paleoclimate proxies in a continuously-monitored natural cave system. *Geochim. Cosmochim. Acta* **75**, 4929–4950Tremaine, D. M.; Froelich, P. N. and Wang Y. (2011) Speleothem calcite farmed in situ: Modern calibration of δ18O and 13C paleoclimate proxies in a continuously-monitored natural cave system. Geochim. Cosmochim. Acta 75, 4929–4950..

Trolier M., White J. W. C., Tans P. P., Masarie K. A. and Gemery P. A. (1996) Monitoring the isotopic composition of atmospheric CO_2: Measurements from the NOAA Global Air Sampling Network. *J. Geophys. Res.* **101**(25), 897–25,916.

Usdowski E. and Hoefs J. (1986) $^{13}C/^{12}C$ partitioning and kinetics of CO_2 adsorption by hydroxide buffer solutions. *Earth Planet. Sci. Ltt.* **80**, 130–134.

Usdowski E., Michaelis J., Böttcher M. E. and Hoefs J. (1991) Factors for the oxygen isotope equilibrium fractionation between aqueous and gaseous CO_2, carbonic acid, bicarbonate, carbonate, and water (19 °C). *Z. Phys. Chem.* **170**, 237–249.

Usdowski E. and Hoefs J. (1993) Oxygen isotope exchange between carbonic acid, bicarbonate, carbonate, and water: A re-examination of the data of McCrea (1950) and an expression for the overall partitioning of oxygen isotopes between the carbonate species and water. *Geochim. Cosmochim. Acta* **57**, 3815–3818.

Vogel J., Grootes P. and Mook W. (1970) Isotopic fractionation between gaseous and dissolved carbon dioxide. *Zeitschrift für Physik* **230**, 225–238.

Watkins J. and Hunt J. (2015) A process-based model for non-equilibrium clumped isotope effects in carbonates. *Earth Planet. Sci. Lett.* **432**, 152–165.

Watkins J. M., Nielsen L. C., Ryerson F. J. and DePaolo D. J. (2013) The influence of kinetics on the oxygen isotope composition of calcium carbonate. *Earth Planet. Sci. Lttrs.* **375**, 349–360.

Watkins J. M., Hunt J. D., Ryerson F. J. and DePaolo D. J. (2014) The influence of temperature, pH, and growth rate on the ^{18}O composition of inorganically precipitated calcite. *Earth Planet. Sci. Lett.* **404**, 332–343.

Watkins J. M., DePaolo D. J. and Watson E. B. (2017) Kinetic fractionation of non-traditional stable isotopes by diffusion and crystal growth reactions. *Rev. Mineral. Geochem.* **82**(1), 85–125.

White, J. W. C., Vaughn, B. H. and Michel S. E. (2015) University of Colorado, Institute of Arctic and Alpine Research (INSTAAR), Stable Isotopic Composition of Atmospheric Carbon Dioxide (13C and 18O) from the NOAA ESRL Carbon Cycle Cooperative Global Air Sampling Network, 1990-2014, Version: 2015-10-26.

Wolthers M., Nehrke G., Gustafsson J. P. and Van Cappellen P. (2012) Calcite growth kinetics: Modeling the effect of solution stoichiometry. *Geochim. Cosomochim. Acta* **77**(15), 121–134.

Yan H., Schmitt A.-D., Liu Z., Gangloff S., Sun H., Chen J. and Chabaux F. (2016) Calcium isotopic fractionation during travertine deposition under different hydrodynamic conditions: Examples from Baishuitai (Yunan, SW China). *Chem. Geol.* **426**, 60–70.

Yumol L. M., Uchikawa J. and Zeebe R. E. (2020) Kinetic isotope effects during CO_2 hydration: Experimental results for carbon and oxygen fractionation. *Geochimica et Cosmochimica Acta* **279**, 189–203.

Žák K., Onac B. P. and Perşoiu A. (2008) Cryogenic carbonates in cave environments: A review. *Quat. Int.* **187**(1), 84–96.

Zeebe R. E. (2011) On the molecular diffusion coefficients of dissolved CO_2, HCO_3^-, and CO_3^{2-} and their dependence on isotopic mass. *Geochimica et Cosmochimica Acta* **75**(9), 2483–2498.

Zeebe R. E. (2014) Kinetic fractionation of carbon and oxygen isotopes during hydration of carbon dioxide. *Geochim. Cosmochim. Acta* **139**, 540–552.

Zeebe R. E. (2020) Oxygen isotope fractionation between water and the aqueous hydroxide ion. *Geochimica et Cosmochimica Act* **289**, 182–195.

Zeebe, R.E.; Wolf-Gladrow, D.A. (2001) CO_2 in seawater: equilibrium, kinetics, isotopes. Elsevier Oceanography Series, Vol. 65. Elsevier, Amsterdam, pp. 360.

Associate editor: Damon A.H. Teagle